



# Seafloor expression of oceanic detachment faulting reflects gradients in mid-ocean ridge magma supply

Samuel M Howell, Jean-Arthur Olive, Garrett Ito, Mark D Behn, Javier Escartin, Boris J.P. Kaus

## ► To cite this version:

Samuel M Howell, Jean-Arthur Olive, Garrett Ito, Mark D Behn, Javier Escartin, et al.. Seafloor expression of oceanic detachment faulting reflects gradients in mid-ocean ridge magma supply. *Earth and Planetary Science Letters*, 2019, 516, pp.176-189. 10.1016/j.epsl.2019.04.001 . hal-02329607v2

HAL Id: hal-02329607

<https://hal.science/hal-02329607v2>

Submitted on 18 Nov 2020

**HAL** is a multi-disciplinary open access archive for the deposit and dissemination of scientific research documents, whether they are published or not. The documents may come from teaching and research institutions in France or abroad, or from public or private research centers.

L'archive ouverte pluridisciplinaire **HAL**, est destinée au dépôt et à la diffusion de documents scientifiques de niveau recherche, publiés ou non, émanant des établissements d'enseignement et de recherche français ou étrangers, des laboratoires publics ou privés.

1 Seafloor expression of oceanic detachment faulting reflects gradients in mid-ocean ridge  
2 magma supply

3  
4 Samuel M. Howell<sup>\*1,2</sup>, Jean-Arthur Olive<sup>3</sup>, Garrett Ito<sup>2</sup>, Mark D. Behn<sup>4,5</sup>, Javier Escartín<sup>6</sup>, Boris  
5 Kaus<sup>7</sup>

6  
7 \*Corresponding author ([samuel.m.howell@jpl.nasa.gov](mailto:samuel.m.howell@jpl.nasa.gov))

8  
9 **Affiliations**

10 <sup>1</sup>*NASA Jet Propulsion Laboratory, California Institute of Technology, Pasadena, CA*

11 <sup>2</sup>*Department of Geology and Geophysics, University of Hawai‘i at Mānoa, Honolulu, HI*

12 <sup>3</sup>*Laboratoire de Géologie, Ecole Normale Supérieure / CNRS UMR 8538, PSL Research University, Paris, France*

13 <sup>4</sup>*Department of Geology and Geophysics, Woods Hole Oceanographic Institution, Woods Hole, MA*

14 <sup>5</sup>*Department of Earth and Environmental Sciences, Boston College, Chestnut Hill, MA*

15 <sup>6</sup>*Marine Geosciences, Institut de Physique du Globe de Paris, CNRS UMR7154, Paris, France*

16 <sup>7</sup>*Institute of Geosciences, Johannes Gutenberg University Mainz, Mainz, Germany*

17    **Abstract**  
18    Oceanic detachment faulting is a major mode of seafloor accretion at slow and ultraslow spreading  
19    mid-ocean ridges, and is associated with dramatic changes in seafloor morphology. Detachments  
20    form expansive dome structures with corrugated surfaces known as oceanic core complexes  
21    (OCCs), and often transition to multiple regularly-spaced normal faults that form abyssal hills  
22    parallel to the spreading axis. Previous studies have attributed these changes to along-axis  
23    gradients in lithospheric strength or magma supply. However, despite the recognition that magma  
24    supply can influence fault style and seafloor morphology, the mechanics controlling the transition  
25    from oceanic detachment faults to abyssal hill faults and the relationship to along-axis variations  
26    in magma supply remain poorly understood. This study investigates this issue using two  
27    complementary modeling approaches. The first consists of semi-analytical, two-dimensional (2-  
28    D) cross-axis models designed to address the fundamental mechanical controls on the longevity of  
29    normal faults. These 2-D model sections are juxtaposed in the along-axis direction to examine the  
30    response of the plan-view pattern of faults to along-axis variations in magmatic accretion in the  
31    absence of along-axis mechanical coupling. The second approach uses three-dimensional (3-D),  
32    time-dependent numerical models that simulate faulting and magma intrusion in a visco-elasto-  
33    plastic continuum. The primary variable studied through both approaches is the along-axis gradient  
34    in the fraction  $M$  of seafloor spreading that is accommodated by magmatism. The 2-D and 3-D  
35    results predict different abyssal hill spacing and orientation, however the plan-view geometry of  
36    self-emerging detachment faults predicted by the 3-D numerical models are well explained by the  
37    juxtaposed 2-D models. This indicates a first-order control by cross-axis effects of changing values  
38    of  $M$ . These models are also shown to explain the along-axis extent and plan-view curvature of the  
39    well-developed 13°20'N and Mt. Dent OCCs (Mid-Atlantic Ridge and Cayman Rise) in terms of  
40    quantifiable along-axis gradients in magma emplacement rates.

41     **1. Introduction**

42       The interplay between magmatism and faulting during seafloor spreading shapes the structure  
43       of mid-ocean ridges (MORs) and the abyssal hills that blanket ocean basins. Globally, seafloor  
44       created at decreasing spreading rates exhibits increasing fault size and rougher topography (e.g.,  
45       Macdonald, 1982). This trend has been interpreted to reflect a change in the partitioning of  
46       magmatism and faulting during seafloor spreading, with slower-spreading segments exhibiting  
47       less plate separation accommodated through magmatic intrusion and more via normal faulting  
48       (e.g., Buck et al., 2005; Cannat et al., 2006; Olive et al., 2015).

49       Likewise, local changes in fault style and seafloor morphology along individual ridge segments  
50       (over along-axis distances of tens-of-kilometers) are also closely linked to changes in magma  
51       supply. For example, a detailed bathymetric analysis of the intermediate-spreading Chile Ridge  
52       revealed that abyssal hill-bounding faults become more prominent toward individual spreading  
53       segment ends, corresponding to inferred decreases in magmatic extension (Howell et al., 2016).  
54       These decreases roughly coincide with a reduction in the extent of partial melting as reflected in  
55       the chemistry of extruded basalts. Analogous along-axis variations in seafloor morphology are  
56       often even more pronounced at slow- and ultraslow-spreading MORs (e.g., Shaw 1992; Sempéré  
57       et al., 1993), where intra-segment variations in crustal thickness—a proxy for magma supply—are  
58       globally maximized (e.g., Cannat et al., 2003; Kuo and Forsyth, 1988; Thibaud et al., 1998).

59       One extreme change in seafloor morphology occurs along sections of slow and ultraslow  
60       spreading segments where abyssal hills associated with short-offset (up to 1-2 km) normal faults  
61       transition to the broad surfaces of oceanic core complexes (OCCs) that are formed by long-lived  
62       detachment faults (e.g., Tucholke et al., 1998; Cann et al., 1997). These detachments may be active  
63       for hundreds-of-thousands to millions of years, exposing tens-of-kilometers of lower crust and

64 mantle rocks along corrugated fault surfaces on the seafloor (**Figure 1a**). Oceanic detachment  
65 faults are involved in the accretion of ~40% of new seafloor along the slow-spreading Mid-Atlantic  
66 Ridge (Escartín et al., 2008; Cann et al., 2015). They also contribute to shaping large extents of  
67 ultraslow-spread seafloor (e.g. Cannat et al., 2006; Dick et al., 2003). As such, they have been the  
68 target of numerous studies in recent years.

69 Analytical models have employed force balance arguments to describe how the mechanical  
70 properties of the brittle crust and upper mantle, or lithosphere, affect fault evolution and  
71 abandonment, thereby controlling their lifespan and average spacing (Forsyth, 1992; Buck, 1993;  
72 Lavier et al., 2000). Buck et al. (2005) combined analytical predictions with dynamic, two-  
73 dimensional (2-D) continuum mechanics models to demonstrate that the size and spacing of  
74 normal faults is directly controlled by the fraction of extension accommodated by the emplacement  
75 of new magmatic material,  $M$ . The subsequent studies by Behn and Ito (2008) and Ito and Behn  
76 (2008) confirmed the relationships between faulting styles and  $M$ , and quantified how  $M$  influences  
77 the morphology of axial valleys and highs. Axial morphology was further addressed by Liu and  
78 Buck (2018), who incorporated feedbacks between axial relief, magma pressure and dike injection  
79 rate through scaling laws and 2-D numerical models.

80 Regarding faulting, the key premise of the above studies is that different values of  $M$  lead to  
81 different opening rates at the magmatic center of the ridge axis (i.e., “neo-volcanic zone”) relative  
82 to the far-field spreading rate. This difference in opening rates controls how fast axis-bounding  
83 normal faults migrate away from the neo-volcanic zone. When  $M$  is high (~1), faults migrate off-  
84 axis rapidly and quickly enter areas of colder, stronger lithosphere where fault slip becomes  
85 mechanically unfavorable. A new fault then forms on-axis, migrates off-axis, and the cycle repeats  
86 to produce closely-spaced faults with minimal offset (**Figure 1a**).

87 As  $M$  decreases toward 0.5, faults migrate off-axis more slowly and stay active longer  
88 producing widely spaced faults that accumulate greater offsets. Where  $M=0.5$ , the rate of off-axis  
89 migration is zero and the fault can remain active indefinitely because it remains in an area of weak  
90 axial lithosphere (**Figure 1b**) (Buck et al., 2005; Tucholke et al., 2008). This theory is supported  
91 by observational evidence that long-lived detachment faults form in regions where magma supply  
92 is subdued (as suggested by positive gravity anomalies, e.g., Tucholke et al., 2008), albeit present  
93 (as indicated by the drilling of extensive gabbro units, e.g., Ildefonse et al., 2007).

94 Thus, extrapolating 2-D model behavior to natural ridge settings suggests that the along-axis  
95 location and extent of detachment faults should coincide with regions of  $M\sim0.5$ . In real systems,  
96 however, the 3-D coupling of stress and deformation likely perturb this ideal and simplified 2-D  
97 picture. Additionally, along-axis gradients in lithosphere strength may affect the development of  
98 “rider blocks” that cover detachment faults and thus impact their seafloor expression (Choi et al.,  
99 2013; Reston and Ranero, 2011; Smith et al., 2008).

100 Modeling of seafloor spreading and faulting at mid-ocean ridges in three dimensions has  
101 matured significantly in the last decade. Simulations of 3-D plate boundary evolution predict that  
102 dynamic instabilities associated with asymmetric accretion could spontaneously form transform  
103 faults and ridge-parallel detachment faults (Gerya, 2010), sensitive to the initial plate boundary  
104 geometry and rheological weakening assumptions (Gerya 2013). Püthe and Gerya (2014) captured  
105 spatial and temporal variations in magmatic and amagmatic accretion for slow and ultraslow  
106 ridges, and Liao and Gerya (2014) found that the generation of oceanic detachment faults in the  
107 late rifting-to-early spreading stage leads to asymmetric seafloor accretion. Differing from the  
108 above work, the study presented here focuses on the effects of along-axis variations in magma  
109 supply on the form and width of OCC’s in a mature seafloor spreading environment.

110 Directly relevant to this study, the effects of along-axis gradients in magma supply were  
111 recently addressed in the 3-D numerical modeling study of Tian and Choi (2017). Their models  
112 predicted long-lived detachments that form near where  $M=0.5$ , but become unstable further along  
113 the ridge where  $M>0.5$ . However, these models were limited by their spatial resolution and did not  
114 clearly produce discrete abyssal hills.

115 In this study, we present the first 3-D models that simulate the transition between an OCC and  
116 well-resolved abyssal hill-scale faults due to along-axis variations in magmatically-accommodated  
117 spreading ( $dM/dy$ ). We note that there are many other important factors that affect seafloor  
118 evolution in 3-D, including segmentation geometry and the associated variations in lithosphere  
119 thickness, as well as their temporal variability. In this study, however, we focus on the mechanical  
120 effects of the magmatic contribution to plate divergence. We begin by predicting the geometry of  
121 faulting along a ridge segment in map view by juxtaposing a series of individual 2-D (cross-axis)  
122 semi-analytical predictions (Buck et al. 2005; Behn and Ito 2008). These results serve as reference  
123 cases to compare with more realistic, fully 3-D numerical models that simulate along-axis  
124 mechanical coupling. Model predictions are then compared with two well-developed detachments  
125 exhibit a relatively simple tectonic structure, are located along linear ridge sections with no  
126 significant offsets, and have a relatively short geodynamic history (they are both active and rooting  
127 at the present-day rift valley).

## 128 **2. Juxtaposed 2-D analytical models of fault evolution in map view**

129 We build upon previous studies (Behn and Ito, 2008; Buck, 1993; Buck et al., 2005; Forsyth,  
130 1992; Lavier et al., 2000; Olive and Behn, 2014; Shaw and Lin, 1996) to construct parametric,  
131 semi-analytical models of fault formation and evolution that are functions of  $M$  and time,  $t$ , in a  
132 2-D section perpendicular to the ridge axis (See Appendix A for the full derivation). We modify

133 existing models to consider that detachment faults and associated abyssal hills occur  
134 predominantly on one side of the ridge axis for extended periods of time. We simulate the accretion  
135 of a seafloor area by juxtaposing numerous 2-D cross-sectional models, each with a different value  
136 of  $M$  ranging from 0.5-0.9. The monotonic variation in  $M$  can be interpreted as a linear variation  
137 in magma supply along a ridge axis, and in this way, the models predict the plan-view geometry  
138 of detachment faults and abyssal hills. We emphasize, however, that each cross-axis slice is truly  
139 2-D because no information is shared between the adjacent slices.

140 The basic behavior of a single 2-D cross-section for a given value of  $M$  follows (see Appendix  
141 A for details). Shortly after a fault is formed, its brittle strength is reduced and the fault becomes  
142 the weakest part of the lithosphere. We assume that fault weakening occurs only through a  
143 reduction of cohesion (e.g., Lavier et al., 2000), and do not incorporate a reduction in the  
144 coefficient of internal friction. The pulling force needed to overcome the frictional resistance of  
145 the fault,  $F_F$ , is thus reduced. As the fault is pushed off-axis by magmatic spreading at the  
146 neovolcanic zone, it encounters thicker lithosphere, rotates to a lower dip, and accumulates finite  
147 displacement, which induces deformation of the adjacent footwall and hanging wall blocks. The  
148 first two effects increase  $F_F$ , while the last effect requires an additional pulling force to bend the  
149 surrounding lithosphere in response to slip on the fault plane,  $F_B$ . The sum of  $F_F$  and  $F_B$  describes  
150 the total pulling force needed to keep the fault slipping. Eventually, the required pulling force  
151 reaches the depth-integrated strength,  $F_I$ , of the un-faulted material at the ridge axis,

$$F_F + F_B \geq F_I. \quad (1)$$

152 This criterion (Eq. 1) is first met when the fault reaches the critical off-axis distance  $x_c(M)$ . At this  
153 point the fault is abandoned and a new fault breaks near the ridge axis, on the same side as the  
154 initial fault. The process repeats with the newly activated fault while the old, inactive one is

156 passively advected further off-axis.

157 We track the temporal evolution of two boundaries: (1) the position  $x_B$  of the footwall cutoff  
158 (FCO), or “breakaway,” which is the very first part of the footwall that was exposed at the seafloor  
159 and is farthest from the ridge axis; and (2) the position  $x_T$  of the hanging wall cutoff (HCO), or  
160 “termination”, which is where the footwall emerges from the seafloor closest to the ridge axis. The  
161 FCO (breakaway) lies on a rigid plate, and therefore migrates away from the ridge axis at the half  
162 spreading rate  $u_{1/2}$ . Its off-axis distance increases with time  $t$  according to:

163 
$$x_B(t) = u_{1/2}t . \quad (2)$$

164 HCOs (terminations) migrate at a slower rate of  $(2M - 1)$  when they are actively slipping ( $x_T < x_c$ ),  
165 and at the half spreading rate when inactive. The location of a HCO (termination) is

166 
$$x_T(M, t) = \begin{cases} \frac{(M - 1)}{2} t_{1/2}, & t < t_c \\ u_{1/2}t - 2x_c \frac{\exp(-M)}{2M - 1}, & t \geq t_c \end{cases} \quad (3)$$

167 where  $t_c$  is the time it takes for the FCO to migrate to the critical distance  $x_c$ ,  $t_c = x_c / ((2M - 1)u_{1/2})$ .

168 The critical distance depends on  $M$  because  $M$  influences how quickly the active HCO migrates  
169 off axis (Eq. 3 for  $t < t_c$ ) relative to the rate of slip on the fault, which in turn influences the pulling  
170 force required to sustain slip  $F_F + F_B$  (see Appendix A). The critical distance also depends on  
171 lithosphere thickness, which is imposed to double over an off-axis distance of  $x=20$  km and remain  
172 constant thereafter, simulating rapid hydrothermal cooling of the lithosphere, and slower,  
173 conductive, cooling beyond 20 km (e.g., Behn and Ito, 2008). For simplicity, in this study we  
174 assume that lithosphere thickness is uniform parallel to the ridge axis.

175 At time  $t=0$ , we consider the system to initiate with a single axially-continuous fault at the neo-

176 volcanic zone and the ridge axis ( $x_B(y, t=0)=0$ ). As the system evolves, the initial FCO  
 177 (breakaway) moves away from the ridge axis in a straight line parallel to the ridge axis at the half-  
 178 spreading rate (**Figure 2a**). Where  $M=0.5$ , the active HCO does not move ( $x_T$  is fixed at zero from  
 179 Eq. 3), marking the center of a long-lived detachment fault. For increasing values of  $M$ , the HCO  
 180 migrates away from the ridge axis at a proportionally increasing rate, and so  $x_T$  increases linearly  
 181 with  $M$  as predicted by Eq. (3) for  $t < t_c$  (**Figure 2a**). The HCO first reaches  $x_c$  at the along-axis  
 182 location where  $M$  is greatest, at which time the HCO becomes inactive and tectonic extension is  
 183 instantaneously transferred to a new fault at  $x=0$ . From this point onward, the inactive HCO moves  
 184 away from the ridge axis at the half-spreading rate (Eq. (3) for  $t \geq t_c$ ).

185 With continued spreading, the location where the fault HCO reaches  $x_c$  migrates progressively  
 186 towards the center of the detachment (the  $M=0.5$  end of the model domain), producing an ever-  
 187 narrowing detachment fault whose HCO is increasingly inclined to the ridge axis. The HCO traces  
 188 out a characteristic curvature in plan-view (Eq. (3) for  $t > t_c$ ), such that the along-axis width of the  
 189 exposed detachment fault surface narrows toward the ridge axis (**Figure 2a**). An equation for the  
 190 half-width of the active “toe” of the detachment (i.e., the along-axis distance between  $y=0$  and the  
 191  $y$ -location where  $x_T=x_c$ ) can be expressed as

$$192 w(t) = x_c \frac{\alpha}{\epsilon} \frac{d}{dy} \left( \frac{M}{\dot{\phi}} \right)^{-1} . \quad (4)$$

193 This equation shows that  $w$  is an inverse function of time for a given along-axis gradient in  $M$ ,  
 194 hence explaining the narrowing of the detachment with time.

195 **Figure 2b** shows the predicted pattern of the cutoffs (active and inactive) for all faults that  
 196 form over a given amount of time. To the side of the active detachment fault, numerous abyssal-  
 197 hill forming normal faults form with a similar characteristic curve. The abyssal-hill faults become

198 more numerous and more closely spaced as  $M$  increases for the reasons predicted by Buck et al.  
199 (2005) and Behn and Ito (2008). While the modeled abyssal hills are more closely spaced and  
200 much more curved than natural ridge systems (e.g. **Figure 1**), the predictions of this first set of  
201 models is useful for distinguishing the effects of along-axis variations in  $M$  in the absence of along-  
202 axis stress and strain coupling from those produced by the full 3-D effects, which is illuminated  
203 by the second modeling effort.

### 204 **3. 3-D Numerical Model**

#### 205 **3.1. Methods**

206 We produce 3-D dynamic models using the computational code LaMEM (Kaus et al., 2016).  
207 This code uses finite differences on a fully staggered mesh with the particle-in-cell method to solve  
208 for conservation of mass and momentum in a visco-elastic-plastic continuum. A more complete  
209 description of the numerical modeling method is presented in Appendix B. The Cartesian model  
210 domain is 80 km in the spreading direction ( $x$ ),  $L=20, 40$ , or 80 km in the along-axis direction ( $y$ ),  
211 and 40 km in the vertical direction ( $z$ ). The domain is discretized uniformly with  $256 \times 64 \times 128$ ,  
212 or  $256 \times 128 \times 128$  elements, respectively (**Figure 3**). We perform 24 simulations consisting of  
213  $\sim 2\text{--}8$  million volume elements and  $\sim 150$  million markers, run on 64–256 processors for  $\sim 10^3$  time  
214 steps in 24–350 hours (Table 1).

215 Our models include four primary material layers, listed here with increasing depth: (1) cold,  
216 low-viscosity ocean, (2) cold, stiff, brittle lithosphere, (3) warmer, high-viscosity ductile material,  
217 and (4) hot, low-viscosity asthenosphere. Layers (2)–(4) are controlled by an Arrhenius  
218 dependence of viscosity on temperature (activation energy is 200 kJ/mol). The ocean layer  
219 viscosity is  $10^{-7}$  times that of the lithosphere to emulate a stress-free boundary condition. Extension  
220 is imposed kinematically by pulling material out through the two sides at a half-spreading rate of

221  $u_{\sqrt{2}}=12.5$  km/Myr, appropriate for many detachment-bearing slow-spreading mid-ocean ridges  
222 (e.g., Tucholke et al., 2008).

223 The lithosphere deforms elastically until differential stress builds to the limit defined by the  
224 Drucker-Prager brittle failure criterion, at which point deformation becomes plastic (see Appendix  
225 B). This failure criterion generates planar volumes of localized shearing that represent fault zones.  
226 The shear planes are further stabilized by reducing brittle strength with accumulated plastic strain  
227 through a reduction of cohesion as in the juxtaposed 2-D models. At the same time, we allow the  
228 plastic strain in the fault zone to heal so that fault strength (cohesion) recovers over a timescale of  
229 20 kyr. These models contrast with prior models that additionally included an evolving coefficient  
230 of friction in fault zones (Gerya, 2013; Püthe and Gerya, 2015; Liao and Gerya, 2015; Gülcher et  
231 al., 2019).

232 We simulate magmatic accretion within a magma injection zone (MIZ) that defines the ridge  
233 axis ( $x=0, y=0-L$ ) (**Figure 3**). Within the MIZ, we impose a velocity divergence of  $2 u_{\sqrt{2}} M(y)/w_{MIZ}$   
234 in a vertical column extending from the seafloor to the base of the axial lithosphere, with a width,  
235  $w_{MIZ}$ , of one element (Eq. B1). This produces a rate of horizontal MIZ widening of  $2u_{\sqrt{2}} M(y)$ . As  
236 the imposed divergence drives markers out of the dike elements, new markers are injected into the  
237 MIZ to keep the marker density above a set value (34).

238 This scheme for magma injection ignores the fact that natural magma emplacement rates can  
239 vary with depth. However, previous studies have shown that fault style is primarily sensitive to  
240 the rate of injection within the brittle lithosphere and not below in the lower-stress regime of ductile  
241 deformation (Olive et al., 2010). Further, when the depth-distribution of magma injection is  
242 calculated from the evolving stress field surrounding the MIZ, the time-averaged magma injection  
243 rates are relatively uniform throughout the lithosphere (Bialas et al., 2010). Our simplified

244 parameterization is thus adequate for the primary objectives of this study.

245 We consider north to be the direction  $y$  increases, and east to be the direction  $x$  increases.  $M$   
246 increases linearly from 0.5 at the southern end ( $y=0$ ) to maximum values of 0.6 to 0.9 at the  
247 northern end ( $y=L$ ). The greatest modeled  $M$  exceeds the maximum value estimated at the Mid-  
248 Atlantic Ridge (Behn & Ito, 2008; MacLeod et al., 2009), ensuring that we capture the full  
249 plausible range.

250 We do not solve the heat equation in our model, rather we impose a temperature structure that  
251 controls viscosity and density in the lithosphere and upper-most asthenosphere. Temperature  
252 increases linearly from 0°C at the seafloor to 600°C at a depth  $H$ , which approximately defines the  
253 thickness of the brittle lithosphere. Along the ridge axis ( $y=0$  to  $y=L$ ), the lithosphere is imposed  
254 to have a uniform along-axis thickness of  $H_0=4$  or 6 km (**Figure 3**), which is comparable to a low  
255 estimate of the seismogenic layer thickness at the axis of slow-spreading ridges (e.g. Parnell-  
256 Turner et al., 2016).

257 The depth to the 600°C isosurface is set to increase linearly with distance  $x$  away from the  
258 ridge axis to a maximum of  $H=2H_0$  at  $x=20$  km. For  $x>20$  km, the base of the lithosphere remains  
259 flat at  $2H_0$ . Below the 600°C-isosurface, temperature increases linearly with depth to 1300°C at a  
260 depth of 1.5  $H$ . This approximately defines the high-viscosity ductile layer. This temperature and  
261 resulting rheological structure is designed to simulate efficient hydrothermal cooling of the  
262 lithosphere to  $x=20$  km off-axis, and less efficient conductive cooling beyond 20 km and below  
263 the brittle lithosphere. The thermal structure is uniform along the ridge axis, and is draped beneath  
264 each point of the model seafloor at each time step so as to preserve a time-invariant (i.e., steady-  
265 state) structure. In this way, we retain precise control over the geometry of the lithosphere and  
266 isolate the effect of along-axis changes in  $M$  on fault behavior (e.g., Behn and Ito, 2008).

267    **3.2. 3-D Model Results and Comparison to 2-D Predictions**

268    The 3-D numerical models exhibit faults that evolve through time, interact, and migrate away  
269    from and along the ridge axis (**Figure 4**). At the onset of extension, an axially continuous fault  
270    forms on one side of the ridge axis. After  $\sim 0.35$  Myr, the hanging wall cutoff (HCO or termination)  
271    remains approximately fixed at  $y=0$ , and a long-lived detachment fault is established, centered at  
272     $y=0$  ( $M=0.5$ ). Further north where  $M>0.5$ , models typically predict shorter-lived faults that migrate  
273    away from the axis ( $t \geq 0.70$  in **Figure 4**). As these smaller faults develop, they may episodically  
274    link at depth with the stable detachment to temporarily form an axially-continuous slip plane (e.g.,  
275     $t=0.93$  and  $1.53$  Myr in **Figure 4**), or they may briefly form on the opposite side of the axis  
276    (**Supplementary Movie S1**). Periodically, a new axially-continuous fault may form on the same  
277    or opposite side of the axis as the detachment, extinguishing the original detachment and adjacent  
278    smaller faults and creating a new detachment system, beginning the cycle over again (**Figure 5,**  
279    **bottom row**).

280    The seafloor in the footwall above the stable detachment fault eventually domes upwards away  
281    from the axis, and the initial HCOs curve in map view along the axis as they become inactive  
282    closer to the segment center at ever decreasing values of  $M$ . This behavior reflects a narrowing of  
283    the actively slipping plane of the detachment with time. At a given time, more gradual along-axis  
284    variations in  $M$  (i.e., smaller gradients,  $dM/dy$ ) tend to produce wider detachments.

285    To understand the 3-D effects of  $dM/dy$  on fault evolution, including along-axis stress and  
286    strain, we compare the shapes of the HCOs with those of the juxtaposed 2-D models of Section 2  
287    through time (**Figure 5**, and **Supplementary Movies S1-S3**). We find that the curved shape of the  
288    initial HCO bounding the detachment fault is very well described by the juxtaposed 2-D models.  
289    This result suggests that the shape of the detachment HCO is not heavily influenced by the 3-D

290 effects of along-axis mechanical coupling, and that the first order influence is the cross-axis effects  
291 of different values of  $M$ .

292 The largest differences between the 3-D and juxtaposed 2-D predictions relate to abyssal hill  
293 geometry away from the detachment (**Figure 2**, **Figure 5**). 3-D models predict abyssal hills to be  
294 form rapidly, with approximately axis-parallel trends, and for only one abyssal hill fault to be  
295 active at a time. The abyssal hills are relatively straight and continuous, and their spacing is  
296 relatively uniform. In contrast, the 2-D models predict that tectonism along the axis occurs on  
297 multiple, highly inclined abyssal hill faults simultaneously (but still with only one active fault for  
298 a given along-axis location). The more dramatic variability in the abyssal hill structures in the 2-  
299 D models reflects the fact that adjacent 2-D models do not interact. In the 3-D models, faults  
300 initiate as planes along the ridge axis and their evolving form reflects some degree of mechanical  
301 coupling in the along-axis direction. Still, the active slip planes of the 3-D faults and associated  
302 HCOs display discontinuities or subtle jogs near the locations predicted by the 2-D models (**Figure**  
303 **5, middle and right column**).

304 **4. Discussion**

305 **4.1. Comparison between models and seafloor observations**

306 Our models provide a simple framework to quantitatively interpret seafloor morphology—in  
307 particular the shape and along-axis extent of OCCs—in terms of along-axis variations in magma  
308 supply alone. Our approach neglects effects related to the presence of transform faults, along-  
309 segment variability in lithosphere thermal structure, composition and rheology, and other  
310 geometrical and tectonic complexities (e.g., obliquity or non-linearity of the ridge axis, presence  
311 of multiple synchronously active faults). The objective is to show that magma supply provides a  
312 satisfactory, first-order explanation for the geometry of OCCs unaffected by ridge-transform

313 intersections.

314 We begin by comparing our model predictions with observations from the well-studied  
315 13°20'N OCC on the Mid-Atlantic Ridge (**Figures 1, 6c, 7**) (Escartín et al., 2017; MacLeod et al.,  
316 2009; Searle et al., 2019; Smith et al., 2006; 2008). This OCC represents the footwall of a  
317 detachment fault that has accumulated ~10 km of offset between its footwall cutoff (FCO,  
318 breakaway) and the easternmost point of its HCO (termination), corresponding to <~0.8 Myr of  
319 extension (Searle et al., 2019). The OCC FCO (breakaway) is a linear ridge that rises ~1 km above  
320 surrounding seafloor (**Figure 7**) and exhibits significant backtilt (~30°) of the volcanic seafloor  
321 due to rotation. Together, these observations are consistent with the hypothesis that the detachment  
322 initiated as a continuous and linear fault spanning >20 km along-axis (Smith et al., 2008; Escartín  
323 et al., 2017, Searle et al., 2019). It is noteworthy that while the OCC FCO does not strike parallel  
324 to the ridge axis, its corrugations—which are reliable indicators of the direction of fault slip over  
325 time—are clearly axis-perpendicular and spreading-parallel (Parnell-Turner et al., 2018). Escartín  
326 et al. (2017) therefore inferred that the FCO initiated with its present-day NNW strike and migrated  
327 westward as the detachment grew.

328 The resulting footwall dome has a topographic amplitude (~1 km) that is well captured by our  
329 3-D simulations (**Figure 6**). The along-axis extent of the dome corresponds to ~50% of the length  
330 of the FCO, which is consistent with the idea that the actively slipping portion of the detachment  
331 narrowed over time, as predicted by both the juxtaposed 2-D and 3-D models. The sub-seafloor  
332 portion of the detachment fault surface has recently been imaged through a high-resolution micro-  
333 seismicity study (Parnell-Turner et al., 2017). The actively slipping surface, as illuminated by the  
334 distribution of earthquakes, does not extend as far north and south as the FCO ridge, and exhibits  
335 a mild curvature in map view (slightly concave to the west) like the HCO of the detachment

336 (Figure 7a). These characteristics are consistent with the behavior of the active slip surface in our  
337 3-D model simulations (Figure 6).

338 In addition, more diffuse micro-seismicity is observed further north in the vicinity of two ~500-  
339 m high scarps striking N-NNE, and separated by ~4 km in the cross-axis direction. These features  
340 are interpreted as the scarps of abyssal-hill forming normal faults, and their relatively narrow  
341 separation and height is consistent with our model predictions in regions of higher  $M$ . In fact,  $M$   
342 values of ~0.6 near the detachment, increasing to ~0.7 near the abyssal hill faults have been  
343 inferred through summation of observed fault heaves (MacLeod et al., 2009) (Figure 7b).  
344 Additionally, a large volcanic cone was emplaced at 13°26'N between these two scarps after their  
345 formation and subsequent flexural back-tilt (Escartín et al., 2017) (Figure 1a, 7a), consistent with  
346 increased magma supply to the nearby axis.

347 Our model thus provides a physically-constrained interpretation for the structure of the  
348 13°20'N OCC and its connection with abyssal hills towards the north. This model is consistent  
349 with the interpretation of Searle et al. (2019), who find discontinuous magnetic patterns around  
350 the OCC that argue against the persistence of a single, segment-long detachment fault. In our  
351 interpretation, the detachment initiated as a ~20-km long normal fault whose HCO became inactive  
352 sooner in the north than in the south due to the greater melt supply, and subsequently migrated off-  
353 axis faster in the north. This prompted new, short-offset abyssal hill-bounding faults to form  
354 sequentially and act as the plate boundary in the north, while connecting with the active, on-axis  
355 detachment fault to the south whose surface expression narrowed through time. We note, however,  
356 that the complexities related to the initial obliquity of the detachment strike relative to the volcanic  
357 axis are not included in, nor predicted by, our modeling effort.

358 To further demonstrate the quantitative agreement between models and observations, we

359 compare the shape of the OCC using the equations arising from the juxtaposed 2-D models. While  
360 the critical distance at which a new fault forms depends on  $M$ , we make the approximation here  
361 that  $x_c$  is constant along-axis such that the solutions for the geometry of fault cutoffs (Eq. 2 and 3)  
362 are fully analytical. This simplification is appropriate given the relatively small variation in  $x_c$   
363 predicted for  $M > 0.6$ , i.e., over most of the model domain (**Figure 2**). The value of  $x_B$  is readily  
364 obtained from a bathymetric map, as it represents the maximum offset on the detachment fault  
365 ( $\sim 10$  km). By substituting Eq. (2) into (3) we can then recover the location of the position of the  
366 HCO (termination),  $x_T$ , relative to the observed location of the FCO (breakaway),  $x_B$ . Inverting Eq.  
367 (5) provides a way to estimate  $x_c$  from the observed spacing between abyssal hills ( $\sim 4$  km) and a  
368 representative  $M$  value in the region where they form (0.7, consistent with the estimate of MacLeod  
369 et al., 2009). This yields an average  $x_c$  of 1.5 km. The resulting detachment geometry, shown in  
370 **Figure 7a**, envelopes the FCO ridge and OCC dome, and accurately predicts the narrowing of the  
371 OCC toe over time. This result provides support that the scaling laws based on the cross-axis  
372 influences of different values of  $M$  (Eq. 2, 3, and 5) adequately explain the plan-form stucture of  
373 an OCC, and that the width of this OCC is plausibly controlled by an along-axis gradient in  $M$   
374 (Figure 8b), consistent with independent estimates (MacLeod et al., 2009).

375 **4.2. Inferring along-axis gradients in magma supply from detachment morphology**

376 To further test the validity of our proof-of-concept method for relating OCC geometry to  
377 gradients in  $M$ , we apply it to an OCC where independent constraints on along-axis variability in  
378 magma supply are available. The Mt. Dent OCC on the ultraslow-spreading Mid-Cayman  
379 Spreading Center (**Figure 8**) (Hayman et al., 2011; ten Brink et al., 2002) exhibits a similar plan-  
380 view shape to that of the 13°20'N OCC along the MAR, and is located in the middle of a linear  
381 ridge section undergoing orthogonal spreading. Van Avendonk et al. (2017) recently conducted a

382 seismic experiment that provides insight into the thickness and nature of the oceanic crust along  
383 the axis of the Mid-Cayman Spreading Center (seismic profile along the dashed yellow line in  
384 **Figure 8**). Their seismic velocity model reveals that the crust—delineated by the 7 km/s P-wave  
385 velocity contour—is thinnest (< 4 km) on-axis near the Mt. Dent OCC, where it likely involves a  
386 large proportion of serpentinized peridotites (Harding et al., 2017). The seismic crust thickens  
387 considerably north and south of the OCC (**Figure 8c**), and the seismic velocity structure becomes  
388 more compatible with that of a basaltic crust 20–30 km away from the detachment where broad  
389 low-velocity zones are imaged at depths between ~3 and 7 km (Van Avendonk et al., 2017).  
390 Crustal thickness peaks have been documented near 18°05'N and at 18°32'N where vigorous  
391 basalt-hosted hydrothermal venting (i.e., the Beebe hydrothermal site: Connelly et al., 2012).  
392 These findings are consistent with Mt. Dent coinciding with a regional minimum in  $M$  at length  
393 scales of 10s of km, as was postulated for the 13°20'N OCC.

394 To extract quantitative constraints on  $dM/dy$  north and south of Mt. Dent, we again make use  
395 of Eqs (2), (3), and (5). The total offset on the OCC is estimated to be  $x_B=16$  km. Determining  $x_c$   
396 here is more challenging than north of the 13°20'N OCC because identifying abyssal hill bounding  
397 faults is not as straightforward. Elongated topographic features north and south of Mt. Dent have  
398 been interpreted as axial volcanic ridges (Van Avendonk et al., 2017), although a tectonic origin  
399 cannot be entirely ruled out. In either case, axial volcanic ridges or abyssal hill-bounding faults  
400 both act as a plate boundary to take up deformation in places where slip on the initial detachment  
401 fault has ceased. In the absence of strong constraints on  $x_c$ , we use the value inferred at 13°20'N  
402 (1.5 km) and estimate the value of  $dM/dy$  that best fits the shape of the Mt. Dent OCC (gray lines  
403 in **Figure 8a**). The corresponding  $M(y)$  profile projected along the seismic profile of Van  
404 Avendonk (2017) is plotted in **Figure 8b**. It predicts an increase in  $M$  from 0.5 to ~0.7 between

405 Mt. Dent and the points of maximum crustal thickness north and south of the OCC.

406 Seismic tomography further reveals that the magma supply decreases beyond these points, as  
407 one approaches the transform faults that bound the Mid-Cayman Spreading Center (Van Avendonk  
408 et al. 2017). Our model thus only applies to the area shown in yellow in **Figure 8b,c** where magma  
409 supply increases away from the OCC. Within this region, the relative increase in  $M$  inferred from  
410 the OCC shape is ~40%, while seismic crustal thickness increases by ~200%. The suggestion of a  
411 greater proportional increase in crustal thickness than  $M$  can stem from the fact that magma  
412 emplacement rates vary drastically with depth, such that a single value of  $M$  averaged over the  
413 whole brittle portion of the magma injection zone may not provide a reliable proxy for crustal  
414 thickness. Olive et al. (2010) showed that OCC growth in numerical models can be achieved over  
415 the full range of possible  $M$  values in the ductile asthenosphere ( $M_D$ ) as long as magma is intruded  
416 in the brittle lithosphere at a relative rate  $M_B \sim 0.5$ . Our model thus only constrains  $M_B$  and  $dM_B/dy$ ,  
417 while crustal thickness reflects a combination of  $M_B$  and  $M_D$ . Additional information on the nature  
418 of the crust is required to efficiently relate the plan-view shape of OCCs and crustal thickness. It  
419 should also be noted that the very notion of seismic crustal thickness may not provide an accurate  
420 proxy for magma supply in this ultraslow-spreading environment where the crust is likely  
421 heterogeneous and complex (e.g., Harding et al., 2017).

422 **4.3. Limitations of the 3-D numerical model and potential future directions**

423 There are several potential areas of improvement in our modeling approach that would allow  
424 more realistic 3-D simulation of the natural behavior of mid-ocean ridge spreading segments.

425 First, to control lithosphere structure both along and across axis, we formally ignore the thermal  
426 evolution of the lithosphere. Solving conservation of energy in future studies and allowing magma

427 injection to affect the thermal structure (e.g., Behn & Ito, 2008) will provide a better understanding  
428 of how natural lithosphere structures control fault morphology and development.

429 Second, we have simplified magma injection processes by assuming that injection rates are  
430 uniform with depth within the lithosphere and prescribed a priori along the ridge axis. Because  
431 injection rates can vary as a function of the local stress field and magma supply (e.g., Behn et al.,  
432 2006; Qin and Buck, 2008), the details of brittle deformation and the surface expression of faulting  
433 would be better captured by allowing dike opening rate (e.g., Bialas et al., 2010) as well the level  
434 that dikes rise in the crust (Liu and Buck 2018) to respond to the local stress field. The next  
435 generation of mid-ocean ridge models should focus on incorporating self-consistent melting and  
436 accretion processes in order to enable more quantitative comparisons between simulated crustal  
437 structure (e.g., faulting and crustal thickness) with seafloor observations.

438 Third, we simplify spontaneous brittle faulting by reducing only cohesion with increasing strain  
439 and assuming a constant fracture healing rate. Recently, Gölcher et al. (2019) demonstrated that  
440 the development of individual OCCs is strongly controlled by fracture healing rates, and their  
441 numerical results deviate significantly from the classic “rolling hinge” model of detachment  
442 faulting. Thus, there is a need for future studies that identify the most appropriate numerical  
443 approaches to fault strength evolution.

444 **5. Conclusions and Perspectives**

445 Both the juxtaposed 2-D models and 3-D dynamic models predict that a linear gradient in  
446 magmatically accommodated extension along a slow-spreading mid-ocean ridge can induce a  
447 transition from long-lived detachment faults to short-lived normal faults. Consistent with previous  
448 2-D studies, long-lived detachment faults are predicted to be centered where the magmatic fraction  
449 of seafloor spreading,  $M$ , is  $\sim 0.5$ . In juxtaposed 2-D models as well as the full 3-D models, the

450 exposed footwall surface of a mature detachment is bound by a curved hanging wall cutoff  
451 (termination) such that the detachment surface is narrowest near the ridge axis, and widens with  
452 distance (or age) away from the axis.

453 Abyssal hill-forming normal faults are predicted to form adjacent to the detachment fault where  
454  $M > 0.5$ . The 2-D models predict many active, highly inclined faults that are inconsistent with  
455 geological observations, while the 3-D models predict only one active, relatively straight abyssal-  
456 hill fault at a time. While the cross-axis effects of varying  $M$  are of first-order importance in  
457 controlling the large-scale structure of OCCs, the along-axis stress and strain coupling is more  
458 important to the detailed structure of the adjacent abyssal hill faults. The 3-D models produce  
459 prominent features that resemble those of natural systems, including detachment faults with  
460 upward doming surfaces, a widening of the detachment surface with distance away from the ridge  
461 axis (as bounded by curved inactive HCO), and multiple abyssal hill-forming faults adjacent to the  
462 detachment that approximately parallel the ridge axis.

463 Smith et al. (2008) describe two possible scenarios for the periodic formation of oceanic core  
464 complexes and abyssal hills in their study of the Mid-Atlantic Ridge (MAR) in the 13° N area: a  
465 “continuous fault” model and a “consecutive fault” model. In their continuous fault model, a single  
466 detachment can span large lengths of individual ridge segments (like that from ~12°50' N to  
467 ~13°40' N). Crust of the median valley floor may be transferred from the hanging wall to the  
468 footwall along faults that root onto the master detachment at depth, creating abyssal hills between  
469 exposed detachment surfaces. This is akin to the “rider block” model (Choi et al., 2013; Reston  
470 and Ranero, 2011), in which the transfer of material onto the footwall (and thus the formation of  
471 abyssal hills vs OCCs) is promoted by greater resistance to continued slip between the footwall  
472 and the rider block material. This implies that  $M$  can be ~0.5 over large distances (like the MAR

473 near 13°N), but that there may be shorter wavelength variations in the mechanical favorability for  
474 continued slip. Such variability could manifest as a change in the coefficient of friction on the  
475 detachment surface (e.g., due to variations in lithology and/or alteration) and/or the dip of the  
476 detachment fault beneath the rider block crust.

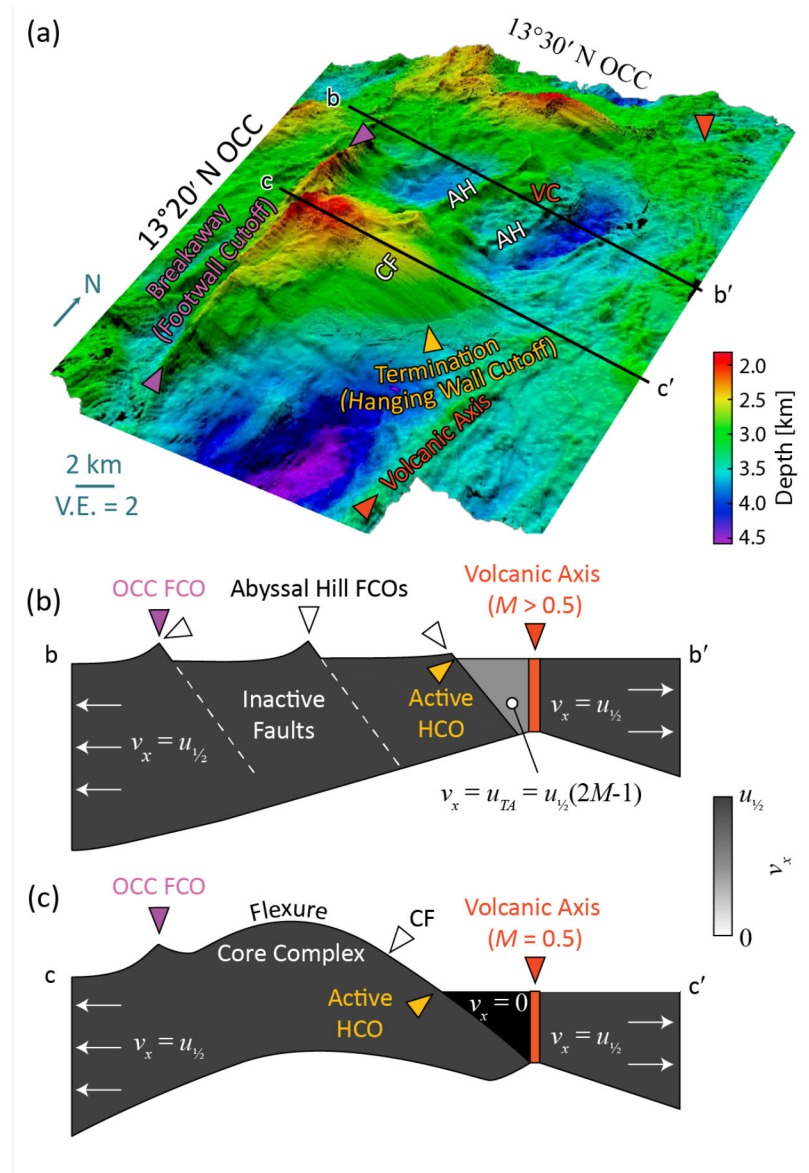
477 Alternatively, the consecutive fault model considers detachment fault surfaces that are  
478 discontinuous along the ridge axis. Smaller normal faults that form abyssal hills do not necessarily  
479 root at the master detachments, thus requiring an along-axis transition from long-lived detachment  
480 faulting to periodic normal faulting—here attributed to variations in  $M$ . The consecutive fault  
481 model is consistent with variations in  $M$  over length scales that are shorter than individual  
482 segments. Along-axis variations in magma supply shorter than the segment scale are well  
483 documented (e.g., Kuo and Forsyth, 1988). When these sub-segment-scale variations occur in  
484 magmatically robust ridge sections with  $M$  well above 0.5 everywhere (e.g., OH1 segment along  
485 the MAR, Hooft et al., 2000; Dunn et al., 2005), detachments cannot form and variations in the  
486 seafloor expression of magma supply gradients are subdued (e.g., Howell et al., 2016). By contrast,  
487 at segments with an overall magma supply close to  $M=0.5$ , small gradients are likely to produce  
488 along-axis transitions in the mode of accretion (detachment vs. abyssal-hill forming faults), as  
489 shown in our models. Indeed, the study by Searle et al. (2019) shows discontinuous magnetic  
490 patterns at the 13°N OCC that seem inconsistent with a single, segment-long detachment fault,  
491 instead supporting the independent evolution of OCCs and detachments.

492 Identifying which OCC-bearing ridge segments are better explained by continuous faulting  
493 (rider blocks) and which are better explained by consecutive faulting (narrowing detachments as  
494 predicted here) may require further analysis of existing seismic data or the collection of new data.  
495 Subsequent analyses must delineate the geometry of internal fault surfaces and distinguish fault

496 surfaces from other sources of crustal heterogeneity. For example, inter-crustal seismic reflections  
497 imaged in an area of seafloor containing an OCC-like structure between the Mid-Atlantic Ridge  
498 and the Canary Islands were interpreted as an OCC fault zone underlying abyssal-hill forming  
499 rider blocks (Reston and Ranero 2011). More such studies on other (younger) OCCs are needed.  
500 Further, new analyses of seismic data should estimate the degree to which crustal thickness varies  
501 along-axis to test for corresponding variations in  $M$ .

502   **Table 1.** Summary of 3-D models run. Columns are respectively lithosphere thickness, axis length,  
 503   minimum and maximum magma supply, magma supply gradient, and mean magma supply.

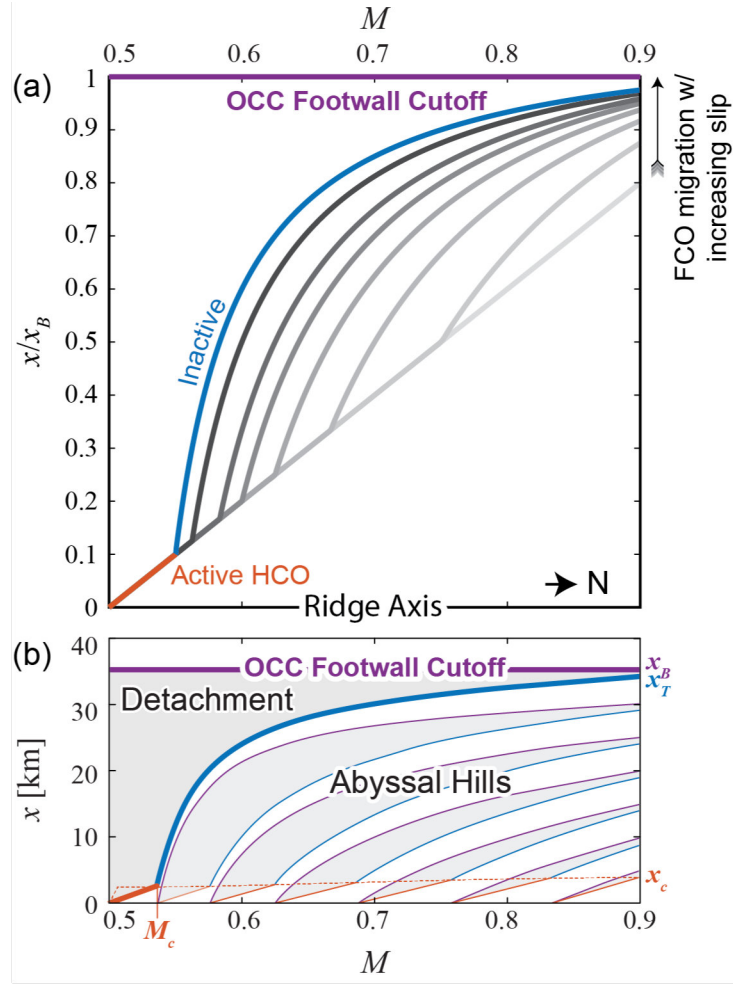
	$H_\theta$ [km]	$L$ [km]	$M_s$	$M_n$	$\Delta M/\Delta y$	$ M $
504 505 506 507 508 509 510 511 512 513 514 515 516	4, 6	20	0.5	0.6	0.0050	0.55
			0.5	0.7	0.0100	0.60
			0.5	0.8	0.0150	0.65
			0.5	0.9	0.0200	0.70
	4, 6	40	0.5	0.6	0.0025	0.55
			0.5	0.7	0.0050	0.60
			0.5	0.8	0.0075	0.65
			0.5	0.9	0.0100	0.70
	4, 6	80	0.5	0.6	0.0013	0.55
			0.5	0.7	0.0025	0.60
			0.5	0.8	0.0038	0.65
			0.5	0.9	0.0050	0.70



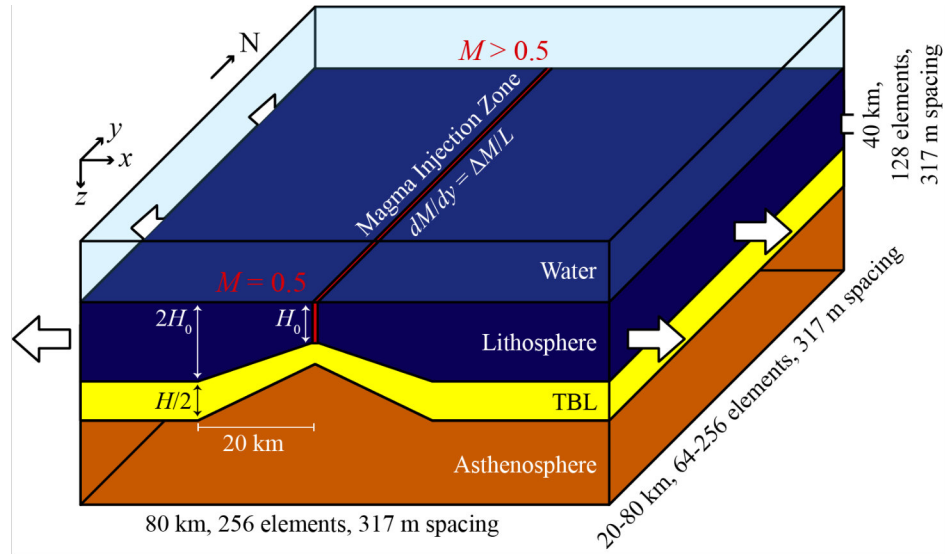
517 **Figure 1.** (a) 3-D perspective view of the bathymetry of the Mid-Atlantic Ridge axis around the  
 518  $13^{\circ}20'N$  and  $13^{\circ}30'N$  oceanic detachments showing the different structural elements associated  
 519 with oceanic core complexes (OCC's). CF marks the corrugated OCC surface, AH marks the  
 520 abyssal hill normal faults, and VC marks an off-axis volcanic cone. Vertical exaggeration is 2. The  
 521 map includes both shipboard and AUV high-resolution bathymetry, acquired during the ODEMAR  
 522 2013 cruise (doi:10.17600/13030070) (Escartín et al., 2017). (b) 2-D schematic of an axis-  
 523 perpendicular cross-section along line b-b' in (a), showing magmatic injection at the ridge axis

524 (orange), and tectonic spreading accommodated by the development and abandonment of short-  
525 throw, high-angle normal faults that form abyssal hills to the west of the ridge axis. (c) Cross-  
526 section beneath line c-c' in (a), showing a single detachment fault that forms the OCC on the west  
527 side of the axis.

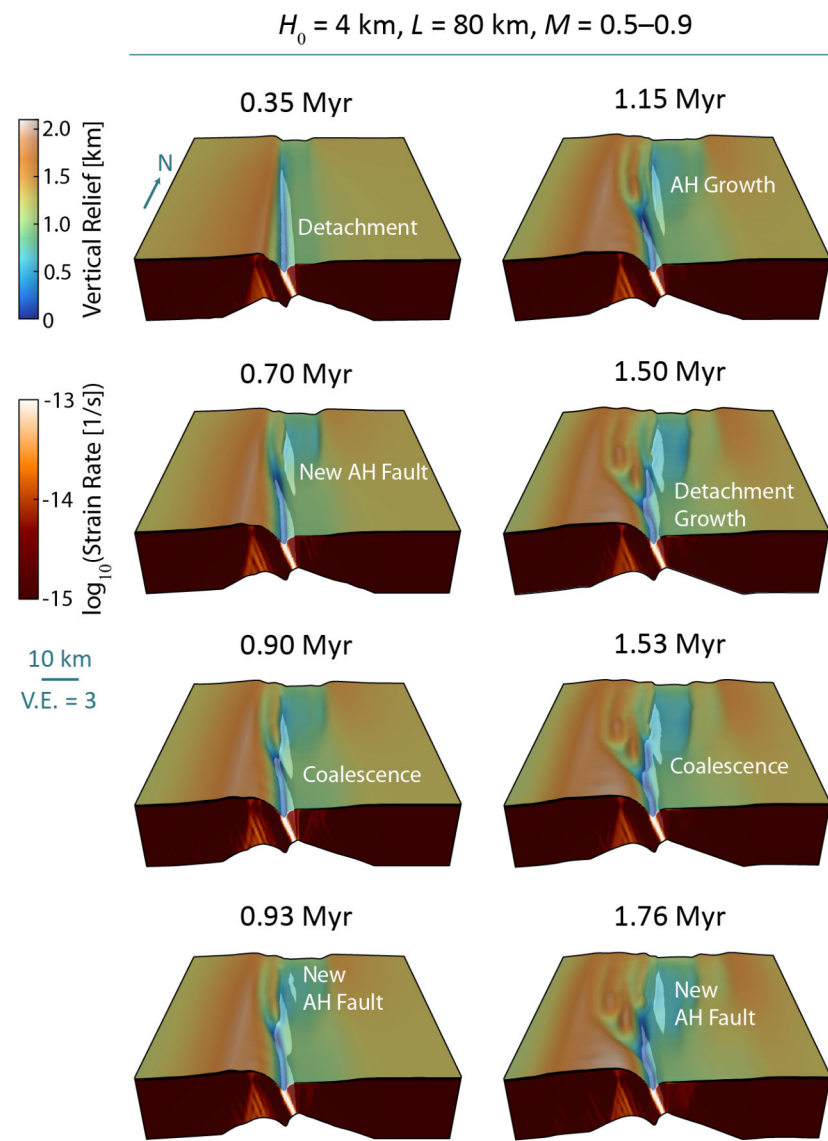
528



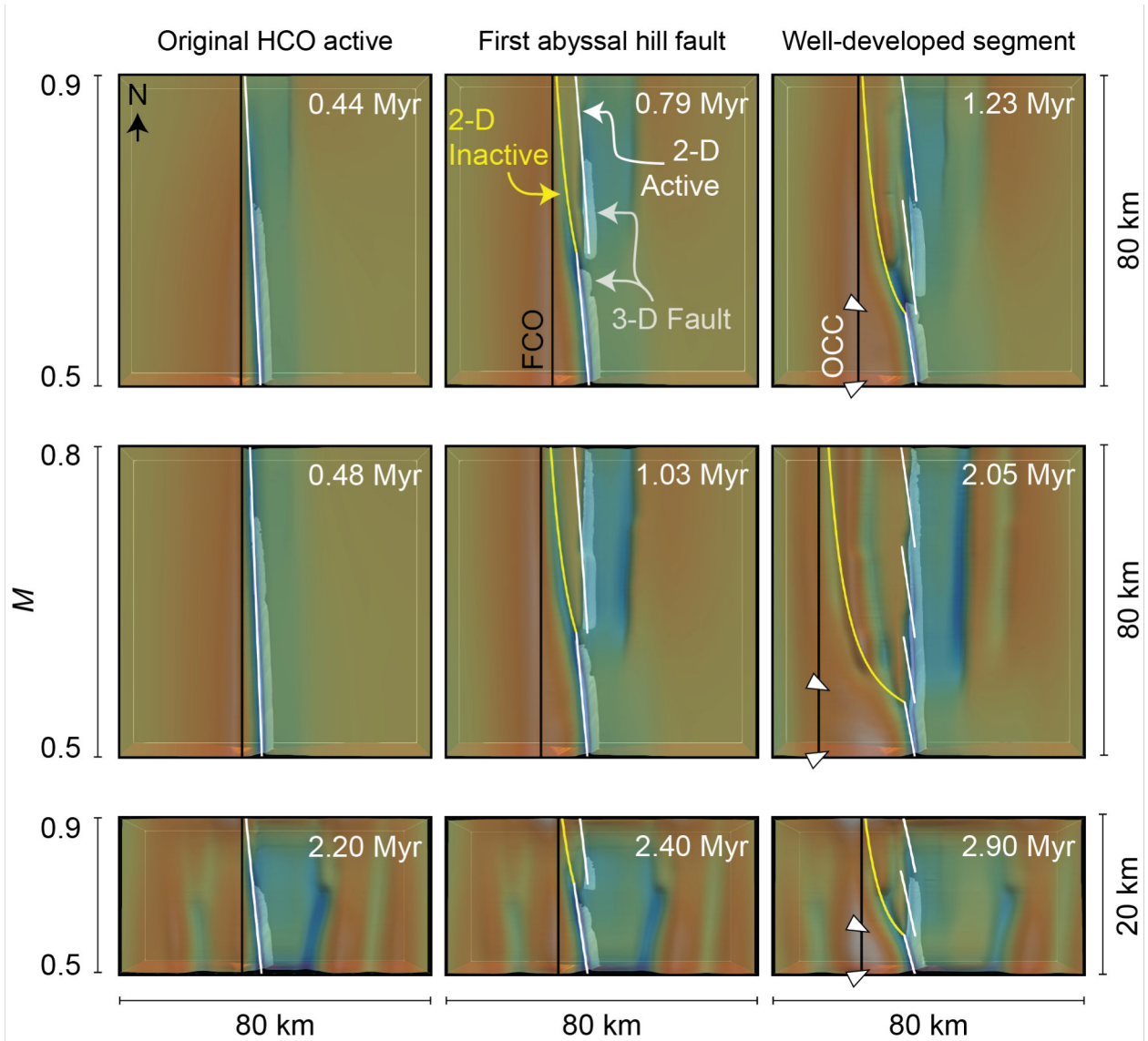
529 **Figure 2.** Example of juxtaposed 2-D semi-analytical solutions of fault geometry in map view  
 530 with  $x$  being the spreading direction and  $M$  varying linearly with distance along a ridge axis (axial  
 531 lithosphere thickness is  $H_0=4\text{ km}$ , and lithosphere thickness  $H$  increase to 8 km at a distance of  
 532  $x=20\text{ km}$ ). (a) Evolution of the inactive HCO (termination) of a single detachment fault with the  
 533 vertical axis normalized by the off-axis FCO (breakaway) distance,  $x_B$ . Grey curves indicate the  
 534 HCO trace for different timesteps with darker colors indicating greater time. (b) Curves show  
 535 actively slipping HCOs (orange) and inactive HCOs (blue) when the FCO (purple) is located at a  
 536 distance  $\sim 10$  times the critical distance after which the detachment HCO becomes inactive  $x_c$   
 537 (orange dashed line). Shaded grey regions represent exposed fault scarps. Note that  $x_c$  shows  
 538 minimal variation over the range in  $M$  for the models studied here (for  $M>0.5$ ).



539 **Figure 3.** 3-D numerical model setup: a low-viscosity “ocean” (transparent blue) overlays a visco-  
 540 elasto-plastic lithosphere (solid blue) defined by temperature that increase from 0° at the surface  
 541 to 600 °C at a depth of  $H$ . The lithosphere transitions to a 1300 °C viscous asthenosphere (orange)  
 542 across a thermal boundary layer (TBL, yellow) between depths of  $H$  and 1.5  $H$ . The depth  $H$  of  
 543 the 600 °C isosurface doubles from  $H_0$  at the ridge axis to  $2H_0$  at a distance 20 km from the axis.  
 544 Material is injected in a narrow “Magma Injection Zone” (MIZ) that defines the ridge axis (red).  
 545 The rate of injection imposes the fraction of total extension accommodated magmatically,  $M$ . The  
 546 left and right model boundaries have zero shear traction and a Dirichlet normal velocity condition  
 547 equal to half spreading rate,  $\pm u_{1/2}$ . The front and back boundaries have zero normal velocities and  
 548 zero shear tractions. The bottom allows for free material in and out flow, the top has imposed  
 549 inflow that conserves water volume, and both boundaries have zero shear tractions.  
 550



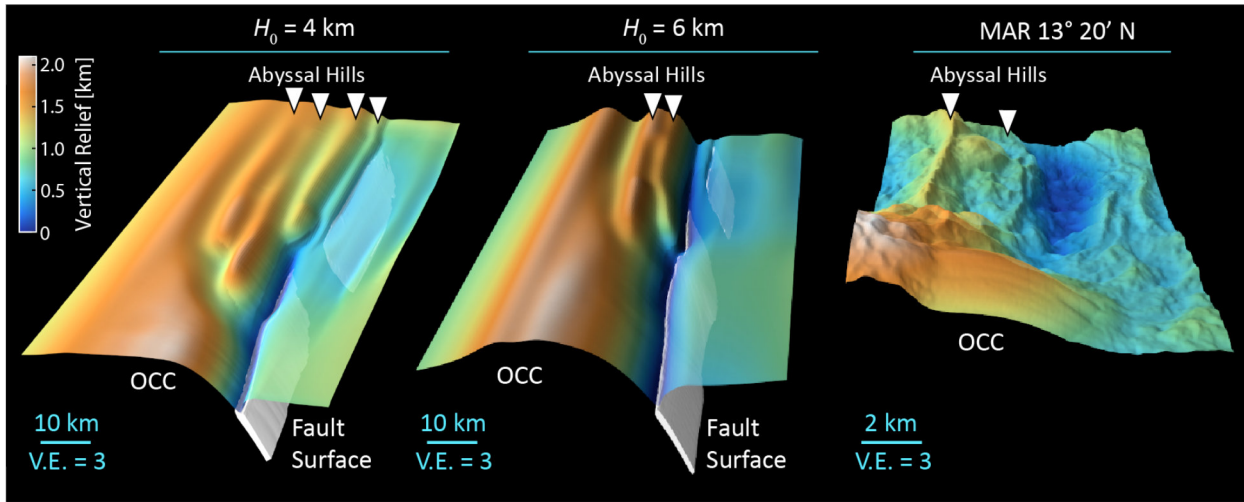
551 **Figure 4.** The evolution of a 3-D simulation ( $H_0=4 \text{ km}$ ,  $L=80 \text{ km}$ ,  $M=0.5\text{--}0.9$ ). A stable  
 552 detachment fault is centered on the south end of the model where  $M=0.5$ , while periodic normal  
 553 faulting produces abyssal hills (AH) further north where  $M>0.6$ . The simulation begins with a  
 554 cycle of abyssal hill formation and growth (0.70 Myr), until eventually the actively slipping plane  
 555 of the abyssal hill fault coalesces with that of the long-lived detachment, forming a single  
 556 continuous fault at depth (0.93 Myr). The cycle then repeats with the formation of a new abyssal  
 557 hill, while the detachment fault remains fixed at the axis. A second episode of fault coalescence  
 558 occurs at 1.53 Myr. Vertical exaggeration (V.E.) is 3:1.



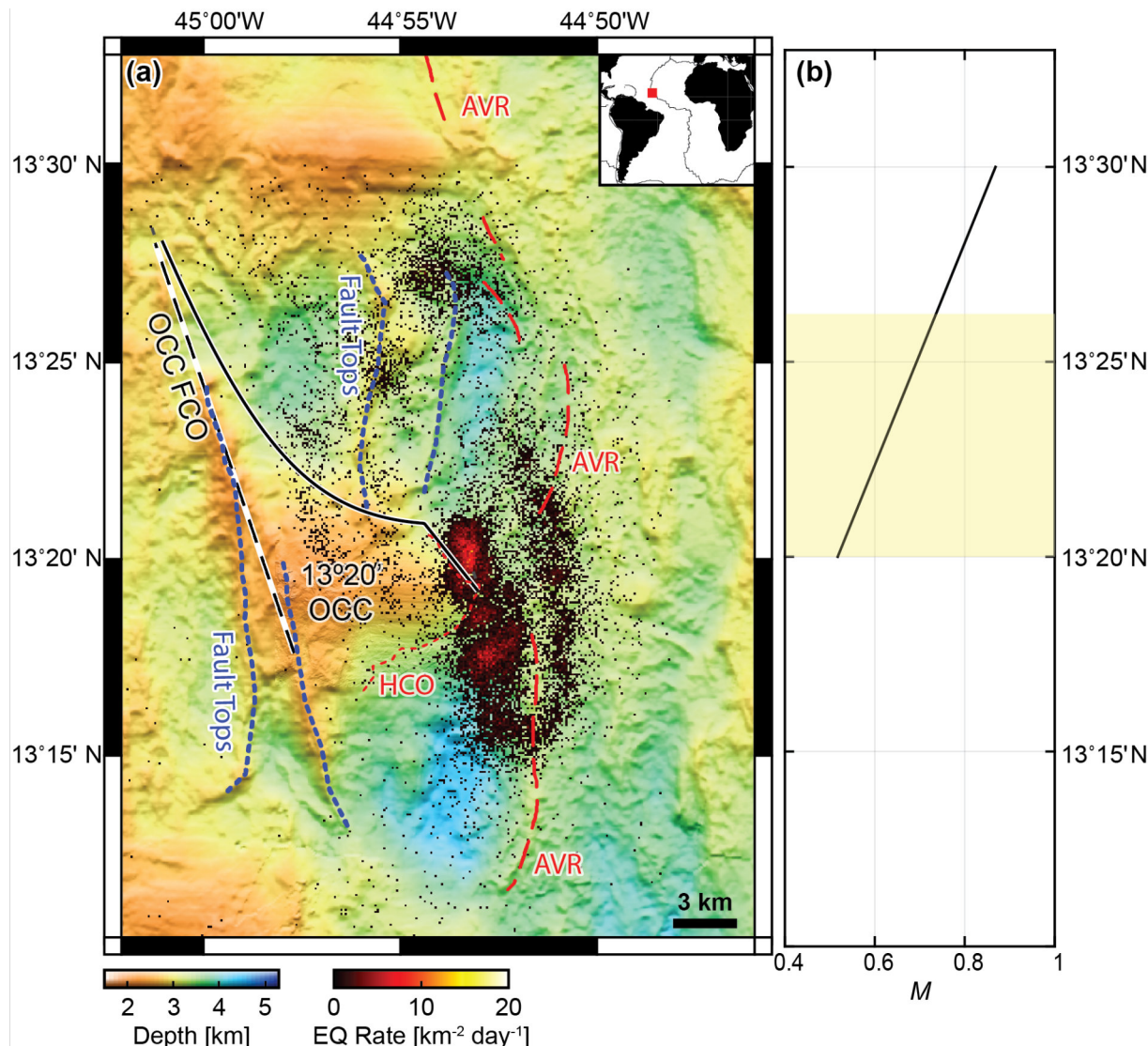
559 **Figure 5.** Rows show shaded bathymetric maps (colored as in **Figure 4**) of model seafloor for  
 560 three separate numerical simulations with  $H_0=4$  km,  $L=80$ ,  $M=0.5-0.9$  (top),  $H_0=4$  km,  $L=80$ ,  
 561  $M=0.5-0.8$  (middle), and  $H_0=4$  km,  $L=20$ ,  $M=0.5-0.9$  (bottom). The model surface is translucent  
 562 to reveal an internal isosurface of the actively slipping fault zone (where cohesion is zero).  
 563 Columns show the time step immediately before the first abyssal hill forms separately from an  
 564 axially-continuous detachment (left), shortly after the first abyssal hill forms (middle), and after  
 565 the second abyssal hill forms (right). The lowermost row shows an active OCC on the west side  
 566 of the ridge axis, with older OCCs visible on either side of the axis. Superimposed on the maps are

567 predictions of the 2-D models of the initial detachment FCO (black line), active fault HCOs (white  
568 line), and the inactive detachment HCO (yellow line). Note the similarity in the along-axis extent  
569 and approximate jogs of the 3-D model's active HCOs with the segmented HCOs predicted by the  
570 juxtaposed 2-D models. The shape of the inactive detachment HCO is especially well explained  
571 by the 2-D solutions (yellow).

572

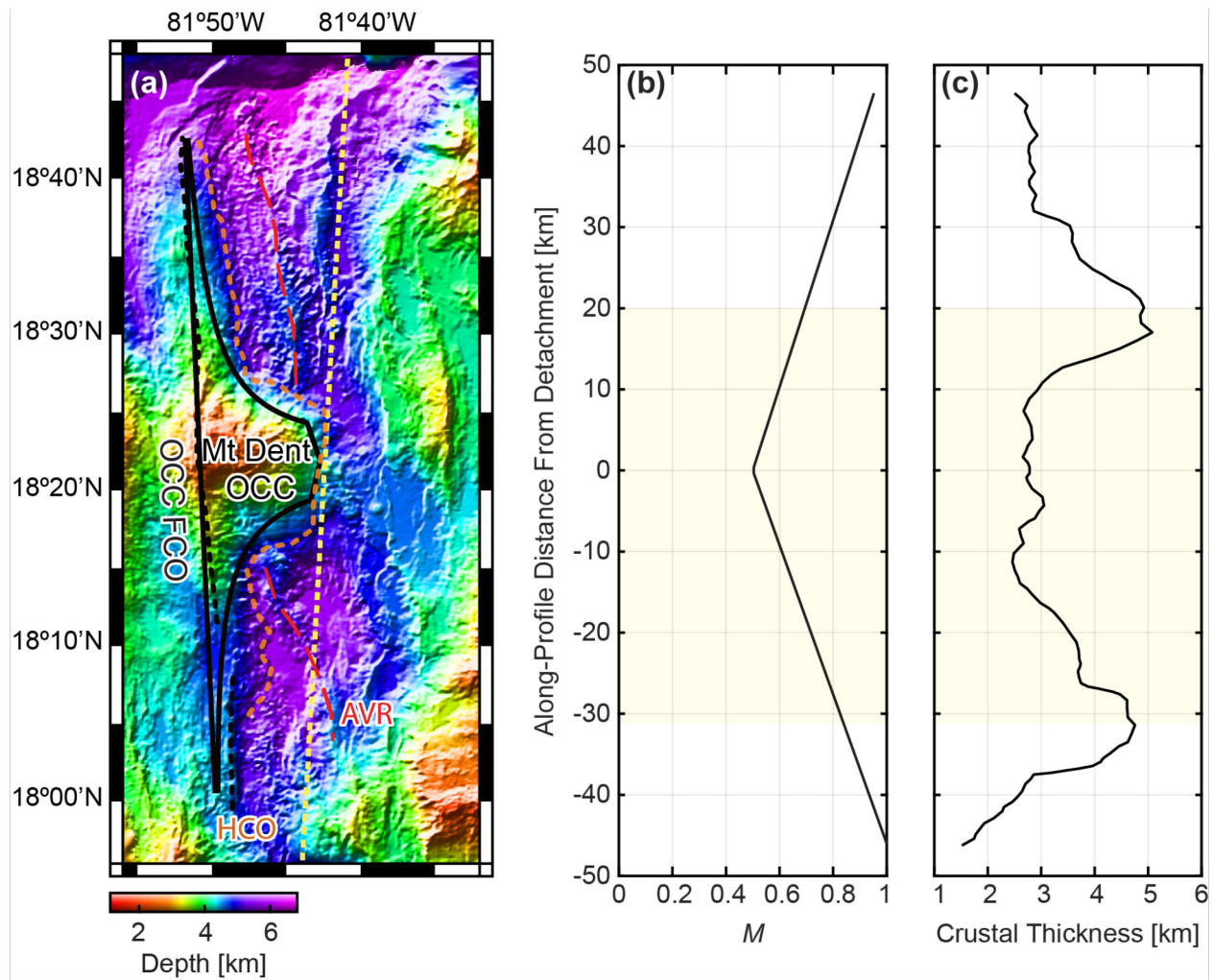


573 **Figure 6.** 3-D perspective views of oceanic detachment faults (south end) transitioning to abyssal  
 574 hill normal faults (north end, white triangles) for models with  $L=80$  km,  $M=0.5\text{--}0.9$ , for  $H_0=4$  km  
 575 (left) and 6 km (center), and of the Mid-Atlantic Ridge segment  $13^\circ 20'N$  (right). The active model  
 576 detachment surface (white isosurface, total cohesion loss) is separate from the newly formed  
 577 normal fault surface beneath the abyssal hills at the time step shown. The curvature of the  
 578 detachment fault HCO is greater in the model with thinner, weaker lithosphere ( $H_0=4$  km). Vertical  
 579 exaggeration (V.E) is 3:1.



589 detachment breakaway (footwall cutoff). The solid black curve marks the inferred location of the  
590 inactive and active termination using Eqs. (2), (3), and (5) assuming  $x_B=10$  km,  $x_c=1.5$  km, and the  
591  $M$  distribution shown in panel (b) projected along the North-South direction. The corresponding  
592 model breakaway is shown as the black-and-white dashed line. (b)  $M$  distribution vs. latitude, used  
593 to visually fit (with the black curve) the inferred geometry of the  $13^{\circ}20'N$  OCC breakaway and  
594 termination. The model variation in  $M$  is roughly consistent with the independent estimate of  
595 MacLeod et al. (2009), who predicted  $M\sim 0.6 - 0.7$  between  $\sim 13^{\circ}21'$  and  $\sim 13^{\circ}25'N$ . The yellow  
596 area marks the along-axis window within which  $M$  likely increases away from the detachment, and  
597 where our scaling laws thus apply. This is because the  $13^{\circ}30'N$  OCC to the North is likely  
598 associated with a local decrease in magma supply not accounted for in the model shown in panel  
599 b.

600



601  
602 **Figure 8.** (a) Bathymetric map of the Mount Dent OCC on the Mid-Cayman Spreading Center  
603 (Connelly et al. 2012). Black lines correspond to predictions of Eqs. (2) and (3) that visually  
604 capture the overall shape of the Mt. Dent termination and breakaway, assuming  $x_B=16$  km and  
605  $x_c=1.5$  km. The termination (hanging wall cutoff) as interpreted by Van Avendonk et al. (2017) is  
606 shown as a pink dashed line, along with the axial volcanic ridge (AVR, red dashed curve), inferred  
607 by the same authors. The black dashed curve marks the crest of the breakaway ridge (footwall  
608 cutoff). (b)  $M$  distribution used to produce the model OCC shape mapped in panel (a). (c) Crustal  
609 thickness along the dashed yellow line plotted in panel (a) inferred from the depth of the 7 km/s  
610 P-wave velocity contour from Van Avendonk et al. (2017). The yellow area marks the along-axis

611 window within which  $M$  likely increases away from the detachment, and where our scaling laws  
612 thus apply. Seismic tomography suggests that the magma supply decreases beyond this region as  
613 one approaches the transform faults that bound the Mid-Cayman Spreading Center to the North  
614 ( $\sim 18^{\circ}50'N$ ) and South ( $\sim 17^{\circ}50'N$ ) (Van Avendonk et al., 2017).

- 615 **References**
- 616 Balay, S., Abhyankar, S., Adams, M., Brown, J., Brune, P., Buschelman, K., Dalcin, L.D.,  
617 Eijkhout, V., Gropp, W., Kaushik, D., 2017. PETSc Users Manual Revision 3.8. Argonne  
618 National Lab.(ANL), Argonne, IL (United States).
- 619 Balay, S., Gropp, W.D., McInnes, L.C., Smith, B.F., 1997. Efficient management of parallelism  
620 in object-oriented numerical software libraries, in: Modern Software Tools for Scientific  
621 Computing. Springer, pp. 163–202.
- 622 Behn, M.D., Ito, G., 2008. Magmatic and tectonic extension at mid-ocean ridges: 1. Controls on  
623 fault characteristics. *Geochem. Geophys. Geosystems* 9.
- 624 Bialas, R.W., Buck, W.R., Qin, R., 2010. How much magma is required to rift a continent? *Earth*  
625 *Planet. Sci. Lett.* 292, 68–78. <https://doi.org/10.1016/j.epsl.2010.01.021>
- 626 Buck, W.R., 1993. Effect of lithospheric thickness on the formation of high-and low-angle normal  
627 faults. *Geology* 21, 933–936.
- 628 Buck, W.R., Lavier, L.L., Poliakov, A.N.B., 2005. Modes of faulting at mid-ocean ridges. *Nature*  
629 434, 719–723.
- 630 Cai, M., Nonaka, A., Bell, J.B., Griffith, B.E., Donev, A., 2014. Efficient variable-coefficient  
631 finite-volume Stokes solvers. *Commun. Comput. Phys.* 16, 1263–1297.
- 632 Cann, J.R., Blackman, D.K., Smith, D.K., McAllister, E., Janssen, B., Mello, S., Avgerinos, E.,  
633 Pascoe, A.R., Escartín, J., 1997. Corrugated slip surfaces formed at ridge-transform  
634 intersections on the Mid-Atlantic Ridge. *Nature* 385, 329.
- 635 Cann, J.R., Smith, D.K., Escartín, J., Schouten, H., 2015. Tectonic evolution of 200 km of Mid-  
636 Atlantic Ridge over 10 million years: Interplay of volcanism and faulting. *Geochem.*  
637 *Geophys. Geosystems* 16, 2303–2321.

- 638 Cannat, M., Rommevaux-Jestin, C., Fujimoto, H., 2003. Melt supply variations to a magma-poor  
639 ultra-slow spreading ridge (Southwest Indian Ridge 61° to 69°E). *Geochem. Geophys.*  
640 *Geosystems* 4, n/a-n/a. doi:10.1029/2002GC000480
- 641 Cannat, M., Sauter, D., Mendel, V., Ruellan, E., Okino, K., Escartín, J., Combier, V., Baala, M.,  
642 2006. Modes of seafloor generation at a melt-poor ultraslow-spreading ridge. *Geology* 34,  
643 605–608.
- 644 Choi, E., Buck, W.R., Lavier, L.L., Petersen, K.D., 2013. Using core complex geometry to  
645 constrain fault strength. *Geophys. Res. Lett.* 40, 3863–3867.
- 646 Connelly, D.P., Copley, J.T., Murton, B.J., Stansfield, K., Tyler, P.A., German, C.R., Van Dover,  
647 C.L., Amon, D., Furlong, M., Grindlay, N., 2012. Hydrothermal vent fields and  
648 chemosynthetic biota on the world's deepest seafloor spreading centre. *Nat. Commun.* 3,  
649 620.
- 650 deMartin, B.J., Sohn, R.A., Canales, J.P., Humphris, S.E., 2007. Kinematics and geometry of  
651 active detachment faulting beneath the Trans-Atlantic Geotraverse (TAG) hydrothermal  
652 field on the Mid-Atlantic Ridge. *Geology* 35, 711–714. doi:10.1130/G23718A.1
- 653 Dick, H.J.B., Lin, J., Schouten, H., 2003. An ultraslow-spreading class of ocean ridge. *Nature* 426,  
654 405. doi:10.1038/nature02128
- 655 Dunn, R. A., Lekić, V., Detrick, R. S., & Toomey, D. R. (2005). Three-dimensional seismic  
656 structure of the Mid-Atlantic Ridge (35 N): Evidence for focused melt supply and lower  
657 crustal dike injection. *Journal of Geophysical Research: Solid Earth*, 110(B9).
- 658 Escartín, J., Mével, C., Petersen, S., Bonnemains, D., Cannat, M., Andreani, M., Augustin, N.,  
659 Bezos, A., Chavagnac, V., Choi, Y., Godard, M., Haaga, K., Hamelin, C., Ildefonse, B.,  
660 Jamieson, J., John, B., Leleu, T., MacLeod, C.J., Massot-Campos, M., Nomikou, P., Olive,

- 661 J.A., Paquet, M., Rommevaux, C., Rothenbeck, M., Steinführer, A., Tominaga, M., Triebe,  
662 L., Campos, R., Gracias, N., Garcia, R., 2017. Tectonic structure, evolution, and the nature  
663 of oceanic core complexes and their detachment fault zones (13°20'N and 13°30'N, Mid  
664 Atlantic Ridge). *Geochem. Geophys. Geosystems* 18, 1451–1482.  
665 doi:10.1002/2016GC006775
- 666 Escartín, J., Smith, D.K., Cann, J., Schouten, H., Langmuir, C.H., Escrig, S., 2008. Central role of  
667 detachment faults in accretion of slow-spreading oceanic lithosphere. *Nature* 455, 790.
- 668 Forsyth, D.W., 1992. Finite extension and low-angle normal faulting. *Geology* 20, 27–30.
- 669 Gerya, T. (2010) Dynamical instability produces transform faults at mid-ocean ridges. *Science*,  
670 329, 1047-1050.
- 671 Gerya, T.V. (2013) Three-dimensional thermomechanical modeling of oceanic spreading initiation  
672 and evolution. *Phys. Earth Planet. Interiors*, 214, 35-52.
- 673 Gülcher, A.J.P., Beaussier, S.J., Gerya, T.V. (2019) On the formation of oceanic detachment faults  
674 and their influence on intra-oceanic subduction initiation: 3D thermomechanical modeling.  
675 *Earth and Planetary Science Letters*, 506, 195-208.
- 676 Harding, J.L., Van Avendonk, H.J.A., Hayman, N.W., Grevemeyer, I., Peirce, C., Dannowski, A.,  
677 2017. Magmatic-tectonic conditions for hydrothermal venting on an ultraslow-spread  
678 oceanic core complex. *Geology* 45, 839–842. doi:10.1130/G39045.1
- 679 Hayman, N.W., Grindlay, N.R., Perfit, M.R., Mann, P., Leroy, S., de Lépinay, B.M., 2011.  
680 Oceanic core complex development at the ultraslow spreading Mid-Cayman Spreading  
681 Center. *Geochem. Geophys. Geosystems* 12.

- 682 Hooft, E.E.E., Detrick, R.S., Toomey, D.R., Collins, J.A., and Lin, J., 2000, Crustal thickness and  
683 upper mantle structure along three contrasting spreading segments of the Mid-Atlantic  
684 Ridge: *Journal of Geophysical Research*, v. 105, no. B4, p. 8205–8226.
- 685 Howell, S.M., Ito, G., Behn, M.D., Martinez, F., Olive, J.-A., Escartín, J., 2016. Magmatic and  
686 tectonic extension at the Chile Ridge: Evidence for mantle controls on ridge segmentation.  
687 *Geochem. Geophys. Geosystems* 17, 2354–2373. doi:10.1002/2016GC006380
- 688 Ildefonse, B., Blackman, D.K., John, B.E., Ohara, Y., Miller, D.J., MacLeod, C.J., 2007. Oceanic  
689 core complexes and crustal accretion at slow-spreading ridges. *Geology* 35, 623–626.
- 690 Ito, G., Behn, M.D., 2008. Magmatic and tectonic extension at mid-ocean ridges: 2. Origin of axial  
691 morphology. *Geochem. Geophys. Geosystems* 9.
- 692 Kaus, B.J.P., A. A. Popov, T. S. Baumann, A. E. Pusok, A. Bauville, N. Fernandez, M. Collignon,  
693 2016. Forward and Inverse Modelling of Lithospheric Deformation on Geological  
694 Timescales. Presented at the NIC Symposium 2016.
- 695 Kuo, B.-Y., Forsyth, D.W., 1988. Gravity anomalies of the ridge-transform system in the South  
696 Atlantic between 31 and 34.5 S: Upwelling centers and variations in crustal thickness. *Mar.  
697 Geophys. Res.* 10, 205–232.
- 698 Lavier, L.L., Buck, W.R., Poliakov, A.N., 2000. Factors controlling normal fault offset in an ideal  
699 brittle layer. *J. Geophys. Res. Solid Earth* 105, 23431–23442.
- 700 Liao, J., Gerya, T. (2015) From continental rifting to seafloor spreading: Insight from 3D thermo-  
701 mechanical modeling. *Gondwana Research*, 28, 1329-1343.
- 702 Liu, Z., Buck, W.R., 2018. Magmatic controls on axial relief and faulting at mid-ocean ridges.  
703 *Earth and Planetary Science Letters* 491, 226–237.

- 704 Macdonald, K.C., 1982. Mid-Ocean Ridges: Fine Scale Tectonic, Volcanic and Hydrothermal  
705 Processes Within the Plate Boundary Zone. *Annu. Rev. Earth Planet. Sci.* 10, 155–190.  
706 doi:10.1146/annurev.ea.10.050182.001103
- 707 MacLeod, C.J., Searle, R.C., Murton, B.J., Casey, J.F., Mallows, C., Unsworth, S.C., Achenbach,  
708 K.L., Harris, M., 2009. Life cycle of oceanic core complexes. *Earth Planet. Sci. Lett.* 287,  
709 333–344.
- 710 Olive, J.-A., Behn, M.D., Tucholke, B.E., 2010. The structure of oceanic core complexes  
711 controlled by the depth distribution of magma emplacement. *Nat. Geosci.* 3, 491.
- 712 Olive, J.-A., Behn, M.D., 2014. Rapid rotation of normal faults due to flexural stresses: An  
713 explanation for the global distribution of normal fault dips. *J. Geophys. Res. Solid Earth*  
714 119, 2013JB010512. doi:10.1002/2013JB010512
- 715 Olive, J.-A., Behn, M.D., Ito, G., Buck, W.R., Escartín, J., Howell, S., 2015. Sensitivity of seafloor  
716 bathymetry to climate-driven fluctuations in mid-ocean ridge magma supply. *Science* 350,  
717 310–313, doi:10.1126/science.aad0715.
- 718 Parnell-Turner, R., Escartín, J., Olive, J.-A., Smith, D.K., Petersen, S., 2018. Genesis of corrugated  
719 fault surfaces by strain localization recorded at oceanic detachments. *Earth and Planetary  
720 Science Letters* 498, 116–128.
- 721 Parnell-Turner, R., R. A. Sohn, C. Peirce, T. J. Reston, C. J. MacLeod, R. C. Searle, N. M. Simão,  
722 2017. Oceanic detachment faults generate compression in extension. *Geology* 45, 923–  
723 926. doi:10.1130/G39232.1
- 724 Poliakov, A.N.B., Buck, W.R., 1998. Mechanics of Stretching Elastic-Plastic-Viscous Layers:  
725 Applications to Slow-Spreading Mid-Ocean Ridges, in: Faulting and Magmatism at Mid-  
726 Ocean Ridges. American Geophysical Union, pp. 305–323.

- 727 Pütthe, C., Gerya, T.V. (2013) Dependence of mid-ocean ridge morphology on spreading rate in  
728 numerical 3-D models. *Gondwana Research*, 25, 270-283.
- 729 Reston, T.J., Ranero, C.R., 2011. The 3-D geometry of detachment faulting at mid-ocean ridges.  
730 *Geochem. Geophys. Geosystems* 12.
- 731 Saad, Y., 1993. A flexible inner-outer preconditioned GMRES algorithm. *SIAM J. Sci. Comput.*  
732 14, 461–469.
- 733 Schouten, H., Smith, D.K., Cann, J.R., Escartín, J., 2010. Tectonic versus magmatic extension in  
734 the presence of core complexes at slow-spreading ridges from a visualization of faulted  
735 seafloor topography. *Geology* 38, 615–618.
- 736 Searle, R. C., MacLeod, C. J., Peirce, C., & Reston, T. J. (2019). The Mid-Atlantic Ridge near  
737 13°20'N: High-resolution magnetic and bathymetry imaging. *Geochemistry, Geophysics,  
738 Geosystems*, 20. doi:10.1029/2018GC007940
- 739 Sempéré, J.-C., Lin, J., Brown, H.S., Schouten, H., Purdy, G.M., 1993. Segmentation and  
740 morphotectonic variations along a slow-spreading center: The Mid-Atlantic Ridge (24°00'  
741 N– 30°40' N). *Mar. Geophys. Res.* 15, 153–200. doi:10.1007/BF01204232
- 742 Shaw, P.R., 1992. Ridge segmentation, faulting and crustal thickness in the Atlantic Ocean. *Nature*  
743 358, 491–493.
- 744 Shaw, W.J., Lin, J., 1996. Models of ocean ridge lithospheric deformation: Dependence on crustal  
745 thickness, spreading rate, and segmentation. *J. Geophys. Res. Solid Earth* 101, 17977–  
746 17993.
- 747 Smith, D.K., Cann, J.R., and Escartín, J., 2006, Widespread active detachment faulting and core  
748 complex formation near 13°N on the Mid-Atlantic Ridge: *Nature*, v. 443, p. 440–444,  
749 doi:10.1038/04950.

- 750 Smith, D.K., Escartín, J., Schouten, H., and Cann, J.R., 2008, Fault rotation and core complex  
751 formation: Significant processes in seafloor formation at slow-spreading mid-ocean ridges  
752 (Mid-Atlantic Ridge, 13 –15° N): *Geochemistry, Geophysics, Geosystems*, v. 9, no. 3, p.  
753 Q03003, doi:10.1029/2007GC001699.
- 754 ten Brink, U.S., Coleman, D.F., Dillon, W.P., 2002. The nature of the crust under Cayman Trough  
755 from gravity. *Mar. Pet. Geol.* 19, 971–987.
- 756 Thibaud, R., Gente, P., and Maia, M., 1998, A systematic analysis of the Mid-Atlantic Ridge  
757 morphology between 15°N and 40°N: Constraints of the thermal structure: *Journal of*  
758 *Geophysical Research*, v. 103, no. B10, p. 24233–24243.
- 759 Tian, X., Choi, E., 2017. Effects of axially variable diking rates on faulting at slow spreading mid-  
760 ocean ridges. *Earth Planet. Sci. Lett.* 458, 14–21.
- 761 Tucholke, B.E., Behn, M.D., Buck, W.R., Lin, J., 2008. Role of melt supply in oceanic detachment  
762 faulting and formation of megamullions. *Geology* 36, 455–458.
- 763 Tucholke, B.E., Lin, J., Kleinrock, M.C., 1998. Megamullions and mullion structure defining  
764 oceanic metamorphic core complexes on the Mid-Atlantic Ridge. *Journal of Geophysical*  
765 *Research: Solid Earth* 103, 9857–9866.
- 766 Van Avendonk, H.J., Davis, J.K., Harding, J.L., Lawver, L.A., 2017. Decrease in oceanic crustal  
767 thickness since the breakup of Pangaea. *Nat. Geosci.* 10, 58–61.
- 768

769   **Acknowledgements:** We wish to thank T. Gerya for his insightful review of this work, and the  
770   editor R. Bendick for her careful treatment of this manuscript. Further, we thank A. Popov for his  
771   role developing and supporting LaMEM, and E. Mittelstaedt and T. Morrow for their early  
772   contributions to this modeling effort. We owe our gratitude to the University of Hawai‘i for use of  
773   their High Performance Computing facility. This study was supported by NSF grants OCE-11-  
774   55098 and OCE-11-54238. Portions of this research were carried out at the Jet Propulsion  
775   Laboratory, California Institute of Technology, under contract with the National Aeronautics and  
776   Space Administration. Government sponsorship acknowledged.

777 **Appendix A: Semi-Analytical Force Balance**

778 The main concepts behind the force-balance-derived solutions for fault spacing are based on  
779 kinematic arguments, and supported by 2-D numerical models, that predict faults are active only  
780 on alternating sides of the ridge at a given time (Behn and Ito, 2008; Buck, 1993; Forsyth, 1992;  
781 Lavier et al., 2000). Near the onset of extension, slip on the active fault causes its strength to  
782 decrease (the above studies assumed a decrease in cohesion), and because it is the weakest point  
783 in the lithosphere, it is the only fault active at that distance  $y$  along the ridge axis. The active fault  
784 accommodates the full fraction of tectonic extension,  $(1-M)$ , on a single side of the ridge axis,  
785 while the magmatism in the neovolcanic zone accommodates the remaining fraction of extension,  
786  $M$ . With time, plate separation accommodated by magma intrusion at the neovolcanic zone causes  
787 the fault to migrate away from the axis into thicker lithosphere, while continued slip on the fault  
788 causes the fault plane to rotate to a shallower dip and the attached lithosphere to bend. These  
789 changes lead to a steady increase in the force required to keep the fault active, and eventually the  
790 tensile stress becomes large enough that it is easier to break a new fault near the ridge axis than  
791 continue slip on the existing fault. At that point, the old fault stops slipping and a new fault takes  
792 up the tectonic fraction of extension, beginning the cycle anew.

793 The creation of the new fault occurs when

794 
$$F_F + F_B^3 F_I , \quad (\text{A1})$$

795 where  $F_I$  is the strength of the intact lithosphere near the ridge-axis (where the new fault forms),  
796 and the force required to keep the old fault active is the sum of the frictional strength of the fault,  
797  $F_F$ , and the force required to bend the adjacent lithosphere,  $F_B$  (Lavier et al., 2000). The force  
798 required to initiate a new fault at the ridge axis is the depth-integrated yield strength of the

799 undamaged axial lithosphere (Behn and Ito, 2008; Forsyth, 1992),  $F_I$ , given by

$$800 \quad F_I = \frac{\mu r g H_0^2 / 2 + H_0 C_0}{\mu \sin(q_0)^2 + \sin(q_0) \cos(\theta_0)}. \quad (\text{A2})$$

801 Here  $\mu$  is the coefficient of rock friction,  $\rho$  is the density,  $g$  is the acceleration due to gravity,  $H_0$  is  
 802 the thickness of the brittle layer at the axis,  $C_0$  is the initial cohesion of the undamaged lithosphere,  
 803 and  $\theta_0$  is the initial fault dip. The force required to overcome friction on the active fault plane is  
 804 similar to (A2), but includes the effects of changing lithosphere thickness  $H$ , fault dip  $\theta$ , and  
 805 accumulated plastic strain  $e_{aps}$ ,

$$806 \quad F_F = \frac{\mu g H^2 / 2 - H C(e_{aps})}{\mu \sin(q)^2 + \sin(q) \cos(\theta)}. \quad (\text{A3})$$

807 The force required to further bend the lithosphere with increasing slip is given by

$$808 \quad F_B = A H^2 (1 - e^{-B h/H}), \quad (\text{A4})$$

809 where  $A$  and  $B$  are empirically-derived elasto-plastic properties of the lithosphere and  $\Delta h$  is an  
 810 increment of fault heave,  $h$  (Lavier et al., 2000).

811 Changes in  $H$ ,  $\theta$ , and  $e_{aps}$  are computed using finite differences and thus are described in terms  
 812 of increments of fault heave as follows. The thickness of the lithosphere is

$$813 \quad H^h = H^{h-1} + D_{af} \frac{\partial H}{\partial x}, \quad (\text{A6})$$

814 where  $\partial H / \partial x$  is the lithosphere thickness gradient in the direction of spreading,  $x$ . Following Behn  
 815 and Ito (2008),

$$816 \quad \frac{\partial H}{\partial x} = \begin{cases} H_0 / 20 \text{ km} & , \quad x \leq 20 \text{ km} \\ 0 & , \quad x > 20 \text{ km} \end{cases}. \quad (\text{A7})$$

817 Fault dip evolves with heave according to,

818 
$$q^h = q^{h-\Delta h} - \frac{\dot{q}}{\dot{h}} \Delta h, \quad (\text{A8})$$

819 where  $\partial\theta/\partial h$  describes the rate of fault rotation with increasing heave (Behn and Ito, 2008). We  
820 impose

821 
$$\frac{\dot{q}}{\dot{h}} = \begin{cases} 5^\circ/\text{km} & , \quad q > 38^\circ \\ 0 & , \quad q \leq 38^\circ. \end{cases} \quad (\text{A9})$$

822 Finally, we can discretize equations Eqs. (A8) and (A9) to write accumulated plastic strain as a  
823 function of incremental fault heave,

824 
$$\epsilon_{aps}^h = \frac{\alpha}{\xi} e_{aps}^{h-\Delta h} + \Delta h \sqrt{\frac{\alpha}{\xi} \frac{1}{Dx} \frac{\dot{\theta}^2}{\dot{\theta}} + \frac{\alpha \tan(q^h)}{\xi} \frac{\dot{\theta}^2}{\dot{\theta}} \frac{\alpha D_{t_h}}{\xi t} + 1} \frac{\dot{\theta}}{\dot{\theta}}, \quad (\text{A13})$$

825 Where  $\Delta x$  and  $\Delta z$  are width and height of the localized model shear band, respectively, used to  
826 calculate incremental strain in the dip-direction.

827 The off-axis distance of the active fault HCO (termination),  $x_T$ , increases by  $\Delta x_T$  for an increase  
828 in fault heave of  $\Delta h$  according to

829 
$$x_T^h = x_T^{h-\Delta h} + D_T \Delta x_T \frac{\alpha M - 1}{2} \frac{\dot{\theta}}{\dot{\theta}}. \quad (\text{A5})$$

830 The increment of heave is related to an increment in time through rate at which the active fault  
831 HCO migrates off-axis,  $u_{TA}$ , which depends on the half spreading rate  $u_{1/2}$  and  $M$ ,

832 
$$u_{TA} = u_{1/2} (2M - 1). \quad (\text{A10})$$

833 The rate at which the fault accumulates heave is the difference between the migration rates at of

834 the fault cutoffs,

835

$$u_{\gamma_2} - u_{TA} = 2u_{\gamma_2}(1-M). \quad (\text{A11})$$

836 This is then used to find the time increment,

837

$$\Delta t_h = \frac{\Delta h}{2u_{\gamma_2}(1-M)}. \quad (\text{A12})$$

838 This is the time increment used with backward finite differences to solve for the evolution of  $H$   
839 (A6, A7), fault dip (A8, A9), and accumulated plastic strain (A13). These quantities then are used  
840 to update  $F_F$  (A3) and  $F_B$  (A4). The time at which the force equation (A1) is met determines  $x_c$ .  
841 The final locations of each of the fault boundaries are then given by Equations (2) and (3) in the  
842 main text.

843

844 **Appendix B: Mathematical and Numerical Method**

845 The configuration and boundary conditions of the 3-D numerical model is shown in **Figure 3**  
 846 and is described in the text. A list of symbol descriptions, units and values is provided in Table  
 847 B1. The above system is modelled mathematically by solving the equations for conservation of  
 848 mass and conservation of momentum for a viscous continuum with zero Reynolds number,

$$849 \quad \frac{\nabla v_i}{\nabla x_i} = \begin{cases} 0 & , \text{ outside of MIZ} \\ \frac{2Mu_{1/2}}{w_{MIZ}} & , \text{ inside of MIZ} \end{cases}, \quad (B1)$$

$$850 \quad \frac{\nabla s'_{ij}}{\nabla x_j} - \frac{\nabla P}{\nabla x_i} - r g_i. \quad (B2)$$

851 Here, repeated indices in a term imply summation over the three index values, denoting the three  
 852 Cartesian directions. In the continuity equation (B1), " $\#$ " and  $\$$  are respectively the Cartesian  
 853 components of velocity and position,  $w_{MIZ}$  is the width of the magma injection zone (here, one  
 854 element wide), and  $u_{1/2}$  is the half-spreading-rate. In the momentum equation (B2),  $s'_{ij}$ ,  $P$ ,  $\rho$ , and  $g_i$   
 855 are respectively the deviatoric stresses, pressure, density, and acceleration due to gravity.

856 Simulating the MIZ is done by imposing a non-zero source term to the continuity equation that  
 857 results in the desired change in velocity across the MIZ. This is preferable to specifying the  
 858 absolute velocity on either side of the injection zone because the imposed divergence allows the  
 859 associated velocities in  $x$  and  $z$  to respond dynamically to lithospheric stresses, and allows faulting  
 860 to occur on one side or both sides of the ridge axis (illustrated in Figure B1).

861 This system of equations is closed with a constitutive law that relates deviatoric stresses to  
 862 strain rates  $\dot{\epsilon}_{ij}$ . The constitutive relation captures ductile (viscous) deformation in the

863 asthenosphere and warmer parts of the lithosphere, the elastic flexure of the lithosphere, and the  
 864 brittle (plastic) failure of lithosphere faults. Ductile deformation is controlled by a creep viscosity,  
 865  $\eta_v$  and is an Arrhenius function of temperature with an activation energy of 200 kJ/mol, and  
 866 elasticity is introduced by assuming the material acts as a Maxwell solid.

867 Finally, brittle failure is simulated by limiting the effective viscosity such that the second  
 868 invariant of deviatoric stress,  $s_{II}$ , never exceeds the yield stress,  $\sigma_Y$ ,

$$869 \quad h_{vep} = \begin{cases} h_{ve} & , s_{II} < \sigma_Y \\ \frac{s_Y}{2\dot{\epsilon}_H} & , s_{II} \geq \sigma_Y \end{cases} \quad (B3)$$

870 The yield stress is determined by enforcing the Drucker-Prager form of the Mohr-Coulomb yield  
 871 criterion,

$$872 \quad \sigma_Y = P \sin(\phi) + C \cos(\phi), \quad (B4)$$

873 where  $\phi$  is the friction angle and  $C$  is the cohesion.

874 The deformation in regions limited by  $\sigma_Y$  is referred to as “plastic” strain, and these deformation  
 875 regions tend to localize in bands that resemble fault zones. This plastic deformation is tracked  
 876 through time and used to calculate an accumulated plastic strain,  $\varepsilon_{aps}$ . We impose a cohesion law  
 877 such that  $C$  decreases linearly with  $\varepsilon_{aps}$  to simulate damage-induced weakening of rock material  
 878 (Poliakov and Buck, 1998),

$$879 \quad C = \begin{cases} 1 - \frac{\alpha e_{ap} - e_{crit,1}}{e_{crit,2} - e_{crit,1}} \frac{C_0}{\dot{\epsilon}} & , \quad e_{crit,1} \leq e_{ap} \leq e_{crit,2} \\ 0 & , \quad e_{ap} \geq e_{crit,2} \end{cases}, \quad (B5)$$

880 where  $C_0$  is the initial cohesion,  $e_{crit,1}$  is the critical strain required for the onset of cohesion loss,

881 and  $\varepsilon_{crit,2}$  is the critical strain required for full cohesion loss. In addition to this weakening  
 882 mechanism, we simulate “healing” of the damaged rock by decreasing the accumulated plastic  
 883 strain between successive time steps  $Dt$  (Poliakov and Buck, 1998),

$$884 \quad e_{aps}^t = e_{aps}^{t-\frac{D\ddot{\alpha}Dt}{\dot{\epsilon} t}} + 1 \frac{\ddot{\alpha}}{\dot{\theta}}^{-1}. \quad (B6)$$

885 The rate of healing is controlled by the timescale,  $\tau$ . Thus, plastic shear deformation tends to  
 886 localize into bands (fault zones) when tectonic plastic strain growth outpaces the time-healing  
 887 decay, and accumulated strain builds to the critical value.

888 ***Numerical aspects***

889 We apply the Flexible-GMRES (Saad, 1993) Krylov method to solve Eqs. B1 and B2,  
 890 preconditioned with a coupled geometric Galerkin multigrid preconditioner that smoothens for  
 891 pressure and velocity simultaneously, with 1/viscosity at the pressure block in the preconditioner  
 892 (Cai et al., 2014).

893 Support for all parallel linear algebra, in the form of matrices, vectors, preconditioners, Krylov  
 894 methods and nonlinear solvers is provided by PETSc (Balay et al., 2017, 1997). Parallelism is  
 895 achieved by spatially decomposing the structured finite difference grid with several DMAD  
 896 objects as provided by PETSc.

897 The simulations were performed using the University of Hawai‘i High Performance  
 898 Computing cluster, which has 178 standard compute nodes consisting of two Intel Xeon E5-  
 899 2680v2 “Ivy Bridge” 10-core, 2.8GHz processors. Each model was run on 64-256 cores distributed  
 900 over 4-13 nodes. The models required approximately 900 time steps, summing to approximately~1  
 901 day of computation time for a mesh resolution of  $256 \times 64 \times 128$  finite difference elements, and

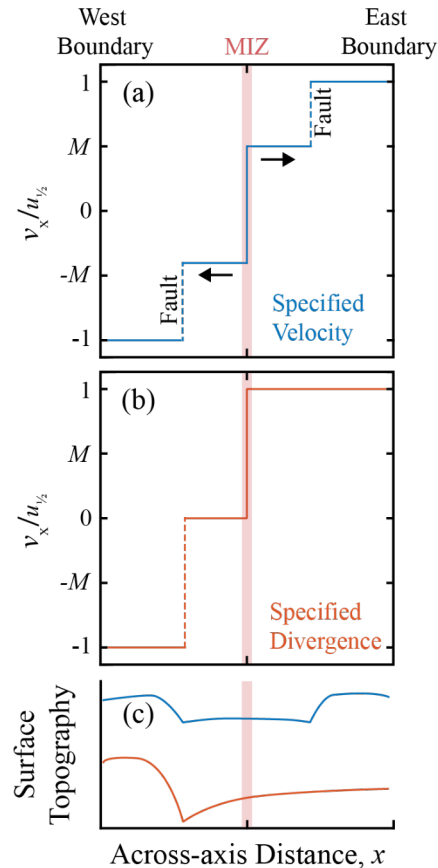
902 14 days of computation time for a mesh of  $256 \times 256 \times 128$ .

903 The multigrid preconditioner was configured with five levels. For the largest models, the  
904 number of elements from the coarsest to the finest level were:  $16 \times 16 \times 8$ ,  $32 \times 32 \times 16$ ,  $64 \times 64 \times 32$ ,  
905  $128 \times 128 \times 64$ ,  $256 \times 256 \times 128$ . The coarse grid solver was a parallel direct solver (`superlu_dist`). The  
906 non-linear SNES solver uses Newton iterations, with the convergence criteria being either a  
907 relative tolerance (`rtol`) of  $10^{-3}$  or absolute tolerance (`atol`) of  $10^{-2}$  and an Eisenstadt-Walker  
908 algorithm, combined with line search (`cp`). The inner linear KSP solver is terminated when relative  
909 tolerance  $10^{-4}$ , an absolute tolerance of  $10^{-3}$ , or 15 iterations are reached. Two smoothening steps  
910 are used at every level of the multigrid algorithm using Chebyshev/SOR iterations.

911 LaMEM (Kaus et al., 2016) is an open source code released under the GNU General Public  
912 License v.3 and may be accessed at <https://bitbucket.org/bkaus/LaMEM>. LaMEM leverages  
913 functionality from PETSc, which can be freely downloaded at <http://www.mcs.anl.gov/petsc>. For  
914 this paper we used the branch `/dike_injection` and commit version `53a3f43`. Input files are available  
915 upon request from the corresponding author.

**Table B1:** Descriptions, values, and units for model parameters.

Symbol	Description	Value	Units
$v_i$	Velocity field		
$x_i$	Cartesian position		
$M$	Fraction of magmatic extension	0.5–0.9	-
$u_{1/2}$	Ridge half-spreading rate	12.5	km/Myr
$w_{\text{MIZ}}$	Magma injection zone width	317	m
$\sigma_{ij}'$	Deviatoric stress		
$P$	Pressure		
$r$	Density	1,000–3,300	kg/m <sup>3</sup>
$g_i$	Gravitational acceleration	9.81	m/s <sup>2</sup>
$\dot{\epsilon}_{ij}$	Strain rate		
$h_v$	Lithosphere creep viscosity	$1\times10^{18}\text{--}1\times10^{24}$	Pa s
$G$	Elastic shear modulus	40	GPa
$\Delta t$	Computational visco-elastic timestep	< 3.9	kyr
$h_{ve}$	Visco-elastic viscosity	< $1\times10^{24}$	Pa s
$z$	Visco-elastic ratio		
$\sigma_Y$	Yield stress		
$C_0$	Initial cohesion	30	MPa
	Friction angle	30	degrees
$e_{aps}$	Accumulated plastic strain		
$e_{crit,1}$	Critical $e_{aps}$ for onset of cohesion loss	0.02	-
$e_{crit,2}$	Critical $e_{aps}$ for full cohesion loss	0.1	-
$t$	Plastic healing timescale	20	kyr
$h_{vep}$	Full visco-elasto-plastic viscosity	< $1\times10^{24}$	Pa s
$H_0$	Axial lithosphere thickness	4, 6	km
$H$	Lithosphere thickness	4–8, 6–12	km



918 **Figure B1:** Schematic of lithosphere velocities,  $v_x$ , for a magma injection zone (MIZ) imposed  
 919 through (a) specified velocity on either side of the MIZ and (b) specified divergence across the  
 920 MIZ. (c) Corresponding cartoons of surface topography for velocity (blue) and divergence  
 921 (orange) specification. Imposing velocities on the sides of the MIZ would force faulting to occur  
 922 on both sides of the ridge axis, whereas imposing a divergence in the MIZ allows faulting to  
 923 respond dynamically, sometimes occurring on one side of the ridge axis and other times occurring  
 924 on both sides.